

Distribution of independent components of binocular natural images

David William Hunter

School of Psychology and Neuroscience,
University of St. Andrews, St. Andrews, Fife, UK



Paul B. Hibbard

School of Psychology and Neuroscience,
Department of Psychology, University of Essex,
Colchester, Essex, UK



An influential theory of the function of early processing in the visual cortex is that it forms an efficient coding of ecologically valid stimuli. In particular, correlations and differences between visual signals from the two eyes are believed to be of great importance in solving both depth from disparity and binocular fusion. Techniques such as independent-component analysis have been developed to learn efficient codings from natural images; these codings have been found to resemble receptive fields of simple cells in V1. However, the extent to which this approach provides an explanation of the functionality of the visual cortex is still an open question. We compared binocular independent components with physiological measurements and found a broad range of similarities along with a number of key differences. In common with physiological measurements, we found components with a broad range of both phase- and position-disparity tuning. However, we also found a larger population of binocularly anticorrelated components than have been found physiologically. We found components focused narrowly on detecting disparities proportional to half-integer multiples of wavelength rather than the range of disparities found physiologically. We present the results as a detailed analysis of phase and position disparities in Gabor-like components generated by independent-component analysis trained on binocular natural images and compare these results to physiology. We find strong similarities between components learned from natural images, indicating that ecologically valid stimuli are important in understanding cortical function, but with significant differences that suggest that our current models are incomplete.

Introduction

A perception of depth is necessary for humans and other animals to understand, interact with, and

navigate around our environment. One of our principal sources of depth information is binocular vision, in which the small differences between the images formed in our two eyes are used to infer the three-dimensional structure of the environment. Although the responses of some neurons in the lateral geniculate nucleus are affected by the images presented to both eyes (Tong, Guido, Tumosa, Spear, & Heidenreich, 1992), it is widely held that the first stages of disparity processing occur in the primary visual cortex (V1; Cumming & DeAngelis, 2001; Parker, 2007; Roe, Parker, Born, & DeAngelis, 2007). Here, cells are found that are tuned to binocular disparity. The disparity sensitivity of these neurons is well characterized by the binocular energy model (Fleet, Wagner, & Heeger, 1996; Ohzawa, DeAngelis, & Freeman, 1997; Prince, Pointon, Cumming, & Parker, 2002; Read & Cumming, 2003). Under this model, the responses of linear Gabor filters are summed between the two eyes, then squared to produce an energy response. Disparity tuning is introduced by summing across filters with different shapes and/or locations of receptive fields for the two eyes.

Physiological studies of the visual cortex have found widespread evidence of cells that respond to binocular stimuli (for detailed reviews, see Howard, 2002; Howard & Rogers, 2002; Neri, 2005; Parker, 2007; Roe et al., 2007). Hubel and Wiesel (1962) studied V1 in cats and found cells that had Gabor-like receptive fields in both eyes. Similar cells have been found in macaque monkeys (Poggio & Fischer, 1977; Prince, Cumming, & Parker, 2002; Prince, Pointon, et al., 2002), sheep (Clarke, Donaldson, & Whitteridge, 1976), and the visual Wulst of the barn owl (Pettigrew & Konishi, 1976). Numerous studies have characterized these cells in increasing detail, in terms of both the responses of individual cells and their distributions.

Citation: Hunter, D. W., & Hibbard, P. B. (2015). Distribution of independent components of binocular natural images. *Journal of Vision*, 15(13):6, 1–31, doi:10.1167/15.13.6.

Differences in the location and/or phase of the receptive fields of simple cells between the two eyes are common, and are generally thought to form the basis for disparity estimation. Position-disparity-tuned cells have receptive fields of the same shape, but with a shift in location, in the two eyes. Evidence for position-disparity-tuned cells has, for example, been found in V1 of the cat (Anzai, Ohzawa, & Freeman, 1999; Nikara, Bishop, & Pettigrew, 1968; Pettigrew, 1972). Conversely, phase-disparity-tuned cells have receptive fields with an identical location, but a difference in their shape, between the two eyes. Specifically, the wave function of the Gabor-like receptive field is shifted in phase in one eye compared to the other. Such cells have also been found in V1 of the cat by Ohzawa and colleagues (DeAngelis, Ohzawa, & Freeman, 1991, 1995; Ohzawa et al., 1990). Subsequently, researchers have found evidence that disparity-tuned V1 cells in both cats and macaques exhibit a mixture of phase- and position-disparity sensitivity (Anzai et al., 1999; Prince, Cumming, & Parker, 2002; Prince, Pointon, et al., 2002; Tsao, Conway, & Livingstone, 2003). It is generally believed that the outputs of these simple cells feed into V1 complex cells according to some variant on the energy model (Fleet et al., 1996; Ohzawa et al., 1997; Prince, Pointon, et al., 2002; Read & Cumming, 2003). Together, these cells are assumed to form the basis for the estimation of differences in the locations of corresponding features across the two eyes, and thus the perception of depth from binocular disparity.

Since binocular cells in area V1 are tuned for orientation and spatial frequency, it is also possible that their tuning for these properties might differ between the two eyes. Indeed, differences in the preferred orientation between eyes have been found for neurons in the macaque cortex and areas 17 and 21a of the cat (Blakemore, Fiorentini, & Maffei, 1972; Bridge & Cumming, 2001; Nelson, Kato, & Bishop, 1977; Wieniawa-Narkiewicz, Wimborne, Michalski, & Henry, 1992). These interocular differences in the orientation tuning of receptive fields are potentially valuable in the encoding of surface orientation. Orientation disparities, defined as differences in the orientation of corresponding features in the two eyes' images, are created when surfaces are slanted away from fronto-parallel. These orientation disparities could therefore be used to determine the orientation of surfaces (Greenwald & Knill, 2009). Although Bridge and colleagues (Bridge & Cumming, 2001; Bridge, Cumming, & Parker, 2001) have argued that the type of response to orientation found in binocular V1 cells is not well suited to the analysis of orientation disparities, psychophysical evidence suggests that they could contribute directly to the perception of depth (Heydt, Adorjani, Hännny, & Baumgartner, 1978; Ninio, 1985). Differences in the size of the corresponding features in

the two eyes' images could play a similar role (Tyler & Sutter, 1979).

While electrophysiological studies have demonstrated a wide variety of disparity tuning in cortical neurons, they do not directly provide any understanding of why disparity is encoded in this way. Significant understanding of the nature of the computations performed by the visual system can be gained from the analysis of typical natural images. The vast majority of natural-image inputs to the visual system are redundant; a recent estimate by Field and Chandler (2012) put this redundancy at 64% in local regions of monocular natural images. This redundancy includes both noise in the imaging system and dependencies within the data. In particular, natural images exhibit significant spatial redundancy; the intensities of neighboring sample locations are not independently distributed. Analysis of these relationships is an important factor in understanding local image structure and how it can be efficiently encoded.

Barlow (1961) proposed that neurons perform an energy-efficient coding of the visual input by removing this redundancy from the signal. Numerous techniques have been applied to samples from natural images to examine ways in which information can be represented efficiently. For example, Olshausen and Field (1996) created a sparse linear decomposition of image patches by applying a Cauchy prior to favor coefficients (responses) with low values. This resulted in a set of "edge-like" basis functions that were spatially localized, oriented, and bandpass. These Gabor-like functions show many similarities in their overall structure to the receptive-field structure of V1 neurons. Similar results have been found by minimizing mutual information between filter outputs (Bell & Sejnowski, 1997) and maximizing the kurtosis of the population response (Hyvärinen, Hurri, & Hoyer, 2009). A detailed analysis of the similarities of these learned filters with monocular V1 simple-cell responses was carried out by van Hateren and van der Schaaf (1998). Again, clear similarities were noted between the distributions of frequency tuning, orientation, and receptive-field size and measurements of these properties in V1 simple cells in the macaque. These results have been taken as evidence that the visual cortex achieves an efficient coding of visual input using components that are independent, exhibit a sparse response to inputs, and capture non-Gaussian spatial relations in the data. Ringach (2002) compared the receptive-field sizes of components from independent-component analysis (ICA) and components generated using sparse coding (Olshausen, 2002) to those measured in cats and monkeys. He found that, in general, both sparse and ICA components had larger, more narrowly tuned features than those observed in physiological measures. Although the image statistics did not successfully

describe the receptive field of simple cells in V1, Ringach did not conclude that the basic principles were flawed as a way of understanding the function of cortical cells.

Methods for the efficient or optimal encoding of information have also been proposed in order to understand the responses of binocular neurons. A range of approaches to this problem have been taken, in each case with a different optimization goal in mind. Li and Atick (1994a) proposed that the brain encodes information in a way that reduces the redundancy present in natural binocular images. Clearly, the images formed in our left and right eyes are very similar; this similarity is a significant source of redundancy in the visual information that we receive. Li and Atick's (1994a) proposal is that binocular information is encoded in a way that decorrelates the two eyes' images by creating two channels, one that additively combines the left and right eyes' views and one that subtracts them. This two-channel structure is supported by psychophysical evidence (D. Chen & Li, 1998; May, Zhaoping, & Hibbard, 2012). Li and Atick combined binocular decorrelation with whitening of the image as a way of encoding binocular information. The resulting binocular filters exhibited disparity tuning that showed a number of similarities to that found in cortical cells.

Burge and Geisler (2014) derived binocular filters that were optimized for estimating disparity in natural images. This was achieved using the accuracy maximization analysis proposed by Geisler, Najemnik, and Ing (2009). Optimal binocular filters were learned for planar samples, with known disparities, created from natural images. Again, the binocular receptive fields of the learned filters were similar in shape to those found in the visual cortex.

ICA has also been applied to binocular images. Here the aim is to maximize the independence of the learned components, and this is attempted through maximization of the kurtosis of responses. A sparse coding of binocular-image patches was created by Hoyer and Hyvärinen (2000) using ICA. This analysis was performed on patches taken from locations around a simulated convergence point in the left and right views. As a result, it focused on features that were close to alignment.

The components that were learned closely resembled Gabor functions for each eye's view, with a similar orientation and frequency for each eye. They were thus very similar in form to the receptive fields of binocular neurons in V1 (Anzai et al., 1999). A disparity-tuning function for each component was calculated. Following Poggio and Fischer (1977), these were then classified as tuned-excitatory, tuned-inhibitory, near, or far cells. Tuned-excitatory cells are those that show a clear response peak at zero disparity. Conversely, tuned-inhibitory cells show a clear trough in their response at

zero disparity. Near and far cells show a peak in response for near and far disparities, respectively. Hoyer and Hyvärinen (2000) found that the majority of their cells were tuned-excitatory, near, or far cells, with a phase disparity close to zero. This feature of the disparity tuning is again remarkably similar to that found in cortical cells. For example, Prince, Cumming, and Parker (2002) showed that the distribution of phase-disparity tuning for V1 cells showed a very clear peak at 0, with a falloff in the number of cells tuned to larger phase differences. Okajima (2004) performed a similar study using difference-of-Gaussian filtered Gaussian noise and natural images using synthetic horizontal displacement. They generated Gabor-like components by minimizing mutual information. Like Hoyer and Hyvärinen, they found components with similar frequency and orientation. Their analysis identified components exhibiting phase disparity, position disparity, and both.

Taken as a whole, these results show that ICA applied to natural binocular images generates components with a number of close similarities to binocular neurons. These results suggest that the responses of binocular neurons to natural images will in turn be sparse and independent. The purpose of the current study is to extend this approach, in order to provide the first detailed qualitative comparison between the components learned by ICA and the responses of binocular neurons.

Our fundamental approach was similar to that of Hoyer and Hyvärinen (2000), in that we performed ICA on patches cut from corresponding locations in the left and right images of binocular pairs. We adapted and expanded on their approach in a number of important ways.

Firstly, Hoyer and Hyvärinen assessed the disparity tuning of their learned components but did not attempt to quantitatively model their receptive fields. While the components analyzed were described as Gabor-like, they were not fitted with Gabor or other functions. In that study, disparity was quantified by measuring the responses of the component to stimuli that consisted of the components themselves, presented with a range of positional disparities. The shapes and relative locations of the components for each eye's input were not assessed. We modeled the components as Gabor filters, in order to allow us to make direct comparisons with physiological data.

The second difference is that this then allows for a more fine-grained assessment of the components' disparity tuning. In particular, modeling binocular receptive fields allows us to directly assess the position- and phase-disparity tuning of each component. This goes beyond the categorization of tuning functions into tuned-excitatory, tuned-inhibitory, near, and far cells. It should be noted that, in the alert rhesus monkey,

tuned-excitatory cells are also found that show clear tuning to either a crossed or an uncrossed disparity (Poggio, 1991; Poggio & Fischer, 1977; Poggio, Gonzalez, & Krause, 1988; Poggio, Motter, Squatrito, & Trotter, 1985; Poggio & Talbot, 1981), and that cells are better viewed as forming a continuum of tuning characteristics rather than falling into these discrete categories (DeAngelis et al., 1991; Freeman & Ohzawa, 1990; LeVay & Voigt, 1988; Ohzawa et al., 1996). Our analysis allows a detailed assessment of the relationship between the tunings to positional and phase disparities, as has been performed for physiological data (Prince, Cumming, & Parker, 2002; Prince, Pointon, et al., 2002).

The third difference is that, as well as assessing tuning for horizontal disparity, we can also assess the tuning for vertical disparity and for disparities in orientation and spatial frequency.

Finally, our study also differed in the way that we sampled from binocular images. Hoyer and Hyvärinen took their samples from an area around simulated fixation points, which were chosen to make the samples from the two eyes relatively similar. This is an important consideration with binocular images, as their statistical properties are spatially nonstationary (Hibbard, 2007, 2008; Liu, Bovik and Cormack, 2008). Since we tend to fixate the same point with each eye, the disparity in the center of the image is expected to be close to zero. As we move away from this point, the range of expected disparities will increase. The dependence of disparity range on eccentricity is reflected in the tuning of the visual system to disparity, as measured in physiological (DeAngelis & Uka, 2003; Durand, Zhu, Celebrini, & Trotter, 2002; Prince, Pointon, et al., 2002) and psychophysical (Hampton & Kertesz, 1983; Qin, Takamatsu, & Nakashima, 2006) studies. The consequence for ICA is that, if we sample from the same image location in each eye, the similarity between the two samples will decrease as we move from the center of the image to more peripheral locations. This will mean that the left and right halves of the components will be expected to be more similar for central locations than for other locations. In the current study we broadened the sample range to 20° (square) using binocular images taken with calibrated cameras (Hibbard, 2008). Our samples are thus more representative of binocular images in general, rather than the special case of samples relatively close to fixation.

The overall aims of the current study were to perform a detailed analysis of the results of ICA applied to natural binocular images, to provide a comparison between the components learned by ICA and the responses of binocular neurons, and to determine the extent to which this approach can provide an explanation of the function of binocular simple cells in the visual cortex.

Methods

Following the methods of Hoyer and Hyvärinen (2000), we processed the images in four stages. Patch pairs were cut from an image set and normalized, followed by a whitening stage and finally the computation of the independent components. In the next section we describe this method and its reasoning. This method is also similar to that used on synthetic patches (Okajima, 2004).

The data set

The methods for capturing and processing the binocular images are described by Hibbard (2008).¹ These methods will have significant effects on the statistics of binocular images. For example, the convergence of the cameras determines how the disparity statistics will vary as a function of the image location. The details of the image-capture process are therefore repeated here. Images were captured using two Nikon Coolpix 4500 digital cameras, harnessed in a purpose-built mount that allowed the intercamera separation, and the orientation of each camera about a vertical axis, to be manipulated. This is a simplification of the situation for human binocular vision, in which there are potentially three degrees of freedom for each eye (rotations about horizontal and vertical axes, as well as the line of sight). The analyses presented here focus on situations in which vergence is approximately symmetrical and elevation is close to zero. In this case, the expected cyclovergence, which is not possible in the camera setup used, is negligible (e.g., Porrill, Ivins, & Frisby, 1999). In all cases, an intercamera separation of 65 mm (representative of the typical human interocular separation) was used. The cameras were oriented so that the same point in the scene projected to the center of each camera's image, so as to mimic the typical human fixation strategy.

Two classes of scene were investigated. In the first, images were collections of natural objects (fruit, vegetables, stones, shells, plants) arranged in “still-life” collections. These were displayed in a Verivide light cabinet, with D65 illumination, and were viewed from a distance of less than 1 m in all cases. The second collection was of outdoor scenes, taken in the quad of St Mary's College in St Andrews (to include trees, flowers, lawns) or on the beach (to include the beach, rocks). Since the cameras were fixated on a target object in each image pair, and a range of distances was sampled, the images contain a range of convergence distances, from approximately 50 cm to 10s of meters.

Images were captured at a resolution of 1600 × 1200 pixels. They were then calibrated to take account of

the characteristics of the cameras. Firstly, images were calibrated using a camera calibration toolkit that is available online (http://www.vision.caltech.edu/bouguetj/calib_doc). This allowed us to correct for lens distortions, calculate the effective focal lengths of the cameras, and transform the images into a “pinhole-camera” model. That is, the spatial location of each pixel in the image is described in terms of the visual direction through the center of the lens that will project onto that pixel. The final resolution of the images was 1 pixel/arcmin of visual angle. The images were also calibrated to take account of the color characteristics of the cameras, by capturing color patches from a Macbeth ColorChecker DC chart, and using these to map RGB camera values to CIELAB values (Hong, Luo, & Rhodes, 2001). Subsequent analyses were performed on the luminance information only.

The images were resized using a bicubic interpolation function, as implemented by MATLAB’s `imresize` command, such that each pixel corresponded to 4 arcmin of visual angle; the effects of this rescaling were subsequently assessed in detail, as discussed later. From the left images, a set of 100,000 image patches at 25×25 pixels was cut from random locations. Another set of image patches was cut from identical locations in the corresponding right images. That is, the samples from the left and right eyes came from the same position in the image, with the same pixel coordinates, rather than from locations necessarily corresponding to the same physical structure in the scene. The input samples to the ICA were created by concatenating the samples from the two images. Hoyer and Hyvärinen (2000) sampled from a 300×300 pixel region around a simulated vergence point, arguing that this matched the converged and focused configuration of typical viewing. As the statistics of binocular disparity (Hibbard, 2007, 2008; Liu et al., 2008) and the disparity tuning of cortical neurons (DeAngelis & Uka, 2003; Durand et al., 2002; Prince, Pointon, et al., 2002) vary with the position in the image relative to the fixation point, it is important to also consider points away from fixation. Therefore, we sampled uniformly from the whole image. As a control condition, to test the extent to which the binocular properties of the components were determined by the binocular redundancy in the images, ICA was also performed on samples drawn separately, from unrelated positions, in the two images.

Normalization and gain

Rather than transmit absolute intensities across the optic nerves, retinal ganglion cells encode and transmit local changes in intensity (Laughlin, 1981; Srinivasan, Laughlin, & Dubs, 1982). We modeled this by

subtracting from each patch its mean intensity (Hyvärinen, 1999; Okajima, 2004; Olshausen & Field, 1996).

We call the i th combined, vectorized image patch $x_i = \{x_{l,i}, x_{r,i}\}$, where $x_{l,i}$ denotes the i th left patch and $x_{r,i}$ the i th right patch. The luminance-centered left image patch is

$$\bar{x}_{l,i} = x_{l,i} - \langle x_{l,i} \rangle, \quad (1)$$

where $\langle x \rangle$ denotes the mean of x . The same method was applied to the right image patches.

By centering the patch we removed the effects of local illumination on a scale roughly the size of the patch. In order to normalize the contrast and remove illumination differences between the two views, we normalized both left and right patches separately, by dividing each vector by its norm ($\|\cdot\|$):

$$\hat{x}_{l,i} = \frac{\bar{x}_{l,i}}{\|\bar{x}_{l,i}\|}, \hat{x}_{r,i} = \frac{\bar{x}_{r,i}}{\|\bar{x}_{r,i}\|}. \quad (2)$$

This represents a linear approximation of the logarithmic functions believed to occur in early vision as measured by Tong et al. (1992) and developed from psychophysical experimentation by Ding and Sperling (2006). Ding and Sperling’s model normalizes input in a nonlinear fashion using ratios of the left/right intensity at particular phases and frequencies. As we are interested in the phase and frequency distributions of binocular images in the current study, we have preferred whole-patch normalization in order to avoid altering those distributions at this stage. Equation 2 has the effect of making each patch vector into a unit vector, thus equalizing patch contrast across both views and between patch locations. Using this equation, contrast ratios are constrained to be 1, whereas Ding and Sperling’s method allows for all possibilities from one-eye dominance to a unitary left/right ratio. This approximation allows us to study the special case of equal left/right intensity. Adding an extra dimension such as intensity ratio would have increased both the complexity of the analysis and the number of components needed to generate accurate distributions.

Most models of binocular neurons assume a linear summation of inputs followed by a nonlinear post-processing step (DeAngelis et al., 1995; Fleet et al., 1996; Hibbard, 2008; Hyvärinen, 1999; Okajima, 2004), consistent with physiological measurements (Anzai et al., 1999; Prince, Cumming, & Parker, 2002; Prince, Pointon, et al., 2002). The left and right components of the patch were then simply concatenated to form the binocular sample:

$$x_i = [\hat{x}_{l,i}, \hat{x}_{r,i}]. \quad (3)$$

The assumptions of the FastICA algorithm (Hyvärinen, 1999) require each sample to be of unit length, so we further normalized the concatenated vectors. As

these vectors were already of unit length, this amounted to a division by $\sqrt{2}$, making no further adjustments to the relative strengths of the left or right signals.

Whitening

Whitening with principal-component analysis (PCA) is an important preprocessing stage in ICA. It removes linear correlations from the data, and in the case of natural-image statistics acts as a low-pass filter (Hyvärinen, 1999). The patch itself acts as a windowing function and a high-pass filter; combined with whitening this acts as a band-pass filter. The normal power spectrum of an image follows a $1/f^\alpha$ curve (where f is the frequency and α is a constant, normally $\alpha \approx 2$); whitening acts to flatten this curve, normalizing the responses at each frequency. As the signal strength is modulated by $\frac{1}{\sqrt{|f^\alpha|}}$ and noise strength is uniform in the frequency domain (assuming Gaussian white noise), noise dominates the signal at high frequencies (Atick & Redlich, 1992). We performed a low-pass filtering to remove the higher noise-dominated frequencies, by truncating the PCA model. A similar role in noise reduction at high frequencies has been proposed for the retina (Atick & Redlich, 1992). We found that 200 eigenvectors generated by PCA on the image patches explained a mean of 86.7% of the variance in the image patches. ICA is performed in the \mathbb{R}^{200} space generated by the eigenvectors. Components were converted back to the image space by applying the inverse of the whitening matrix.

Independent component analysis

ICA attempts to find a linear decomposition of the data such that each component is maximally independent. We used the FastICA method of Hyvärinen (1999), as it is rapid and generally converges. The algorithm uses gradient descent in an attempt to find the components with the minimum mutual information, using kurtosis as a measure of independence. It should be noted that a general limitation of this approach is that it is not guaranteed to minimize dependencies. This will only be achieved if the samples are a linear superposition in independent, heavy-tailed sources. We used a hyperbolic tangent as the derivative of the nonlinearity and initialized the weights from a random Gaussian distribution. The number of components generated by the algorithm is restricted by the number of eigenvectors generated by the whitening stage. We used 200 eigenvectors from the whitening stage; the same number of independent components were then generated by the FastICA algorithm. The components were converted from the PCA-generated

eigenvector space back into image space by applying the inverse of the whitening matrix. In total, 100,000 binocular image patches were used to train the ICA model, cut from uniformly random locations from 139 left/right image pairs. In order to calculate accurate distributions of the components, we repeated the component generation 200 times using different patch sets (from the same images) each time, thus producing 40,000 components from which reasonably accurate histogram distributions could be calculated.

The meaning of the ICA components

It should be noted that ICA suffers from some limitations. Firstly, as PCA is frequency-bandwidth limited, the resulting components are also frequency-bandwidth limited. This limits the range of frequencies that can be observed and results in components that are more narrowly tuned in frequency than might otherwise be observed (Ringach, Sapiro, & Shapley, 1997). As a consequence of the oriented edge-like structure of the components, we also expect them to be narrowly tuned in orientation. While the frequency content of the components will be restricted, there is no reason to believe that the phase will be substantially altered, as PCA is not limited in phase. Secondly, unlike in PCA, the components are not ordered. Thirdly, there is no test for statistical significance. Fourthly, the algorithm assumes both noiseless input and no output noise. Finally, the algorithm is not particularly robust to initial starting conditions (Hyvärinen, 2011).

A consequence of these issues is that it is not trivial to determine the explanatory power of a given component in the same way that we can for a PCA component. Given the sparse nature of the algorithm, it is conceivable that a component will explain only a small amount of data peculiar to a particular sample set, rather than being a useful descriptor of the general population. This is especially true if noise is present in the input (Hyvärinen, Sarela, & Vigário, 1999). An indirect method to determine the explanatory power is to generate numerous ICA models and check for recurring similar components (Himberg, Hyvärinen, & Esposito, 2004). As our analysis looks at overall trends in the calculated components rather than at individual components in detail, we did not attempt to validate individual components. Instead we calculated 200 separate ICA models using different image patches, with 200 components in each model, thus generating 40,000 components in total. Highly similar and thus significant components will form clusters in this analysis. Nonsignificant components will appear as outliers. Not all the potential independent components will be found, since ICA is restricted to an arbitrary

number of components by the PCA preprocessing stage—in our case, 200.

The distributions of components can be argued to show the relative abundance of a particular independent feature in the binocular-image data. High-prevalence components will form clusters, and can thus be thought of as more prevalent in the data than low-prevalence components. It should be noted that, while repetition of the ICA computation will allow the significance of highly abundant components to be qualitatively determined, it will not readily lead to the discovery of less abundant components, as the highly abundant components will simply be recalculated in each iteration. It should also be noted that the components generated by recalculation are not independent or orthogonal, as the independence constraint is only applied between components generated by a single FastICA computation. However, general trends in the data should be captured.

Fitting Gabor functions

To fit Gabor functions to each of the components, we followed the methods of Okajima (2004), Prince, Cumming, and Parker (2002), and Prince, Pointon, et al. (2002). We fitted Gabor functions separately to each of the left and right view parts of each component by minimizing the L^2 -norm between the function and the component. The 2-D Gabor function is defined as

$$\begin{aligned} g(x, y; \theta, f, \phi, \sigma_w, \sigma_h, \psi) &= w(x, y, \sigma_w, \sigma_h, \psi) c(x, y, f, \phi, \theta) \\ &= \exp\left(-\frac{x'^2}{2\sigma_w^2} - \frac{y'^2}{2\sigma_h^2}\right) \cos(2\pi\hat{x}f \\ &\quad + \phi), \end{aligned} \quad (4)$$

$$\hat{x} = x\cos\psi - y\sin\psi$$

$$\hat{y} = x\sin\psi + y\cos\psi$$

$$\hat{x} = x\cos\theta - y\sin\theta.$$

The Gabor function consists of two components: a wave-generating function $c(x, y, f, \phi, \theta)$ and the windowing function $w(x, y, \sigma_w, \sigma_h, \psi)$ that constrains it in window space. The wave-generating function describes a cosine pattern with frequency f and phase ϕ , this pattern is rotated about the origin by an angle θ . The windowing function constrains the image-space span of the wave-generating function to a Gaussian window of width σ_w and height σ_h ; this window is rotated independently of the wave function by ψ . Previous authors have fixed $\theta = \psi$, such that the windowing function rotates with the wave-generating function (Prince, Cumming, & Parker, 2002). However, we have removed this constraint to allow the Gabor fitting function to describe a greater range and variety

of Gabor-like components. All the Gabor functions are centered at 0 and generated over a two dimensional image $x = [-n/2 : n/2]$ and $y = [-n/2 : n/2]$, where n is the size of the component patch.

In order to match the Gabor function to our component patches, we must add horizontal and vertical displacement terms h and v . Our equation becomes

$$\begin{aligned} G(x, y; h, v, \theta, f, \phi, \sigma_w, \sigma_h, \psi, s) \\ = g(x - h, y - v; \theta, f, \phi, \sigma_w, \sigma_h, \psi) s, \end{aligned} \quad (5)$$

where s is a scaling parameter that models the amplitude of the Gabor function. The parameters of the model were fitted to the data using the Nelder–Mead simplex method (Nelder & Mead, 1965) initialized with a genetic algorithm, using MATLAB's implementation.

Gabor symmetry

As a result of numerous symmetries linking the parameters of the 2-D Gabor function (Equation 4), they are only independent within a particular range.

Rotating the wave function of the Gabor (θ) by π radians is equivalent to reflecting the phase ϕ about 0—i.e., $G(\dots; \theta, \phi, \dots) = G(\dots; \theta - \pi, -\phi, \dots)$. The other parameters have been omitted here for clarity.

Interaction of phase and position shifts

Changes in the spatial location of stimuli can be encoded by Gabor functions by two methods, a phase shift and a position shift. The phase shift is encoded by varying the phase parameter ϕ , the position shift by varying v and h in the direction parallel to the wave-generating function. Phase shifts can be converted to position shifts, and vice versa, by

$$|v\cos\theta - h\sin\theta| = \frac{\phi}{2\pi f} \quad (6)$$

in the range $-\pi < \phi < \pi$. The notation $|\cdot|$ indicates the magnitude of the vector, and the cos and sin terms rotate the shifts into the orientation of the wave-generating function. Equation 6 is derived from the well-known Fourier shift theory. While Equation 6 maps phase and position in the wave-generating function c , phase- and position-shifted Gabor functions differ in terms of the windowing function w . For example, an even-phase Gabor phase-shifted by $\pi/2$ radians will become odd, but an even-phase Gabor function shifted in position by an amount equivalent to $\pi/2$ radians (by Equation 6) will still be even phase.

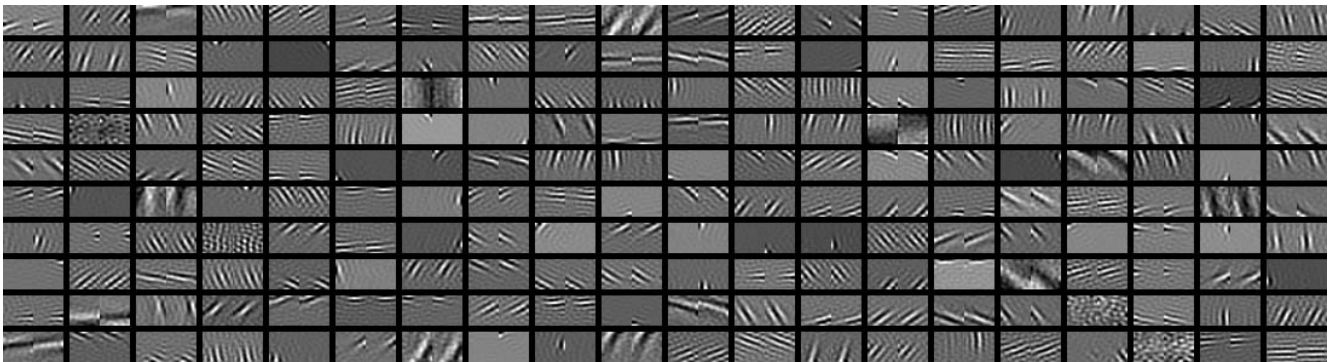


Figure 1. Example of components generated by ICA. Two hundred components generated by a single batch are displayed. The left half of each component corresponds to the left view, the right half to the right view. The Gabor-like components are clearly visible in most components.

Results

Figure 1 shows the results of applying the FastICA algorithm to 100,000 binocular image patches taken from 139 image pairs. In each batch, 200 components are generated; all 200 are shown. Across the 200 runs, the PCA whitening process explained on average 86.7% of variance in the image patches. Each patch shows the concatenated left/right parts of the components. Pairs of Gabor-like components are clearly visible, exhibiting a wide range of orientations, frequencies, and locations.

Accuracy of fitting

The process of generating the ICA components contains many elements that depend on random processes. The patches are sampled from uniformly distributed random locations, and the ICA algorithm iterates from a normally distributed random initial state. The accuracy of the fitting of the Gabor functions can be assessed in terms of both their trueness (lack of bias) and their precision. As the distributions we are interested in are not a priori known, we cannot directly assess their trueness; we can, however, estimate their precision using a bootstrapping technique. This will illustrate the range of distributions produced by this method and allow us to estimate confidence intervals for the distributions. Unlike the overall process, the trueness of the Gabor-fitting subprocess can be evaluated by comparison with synthetic image patches showing Gabor functions with known ground-truth values. If these are sufficiently accurate, we can have some confidence in the accuracy of the values of Gabor functions fitted to components generated by the ICA. We will first describe the process of assessing the trueness of the Gabor-fitting function, then the boot-

strapping we used to generate confidence intervals for the overall process.

In order to assess the trueness, we generated 400 Gabor functions by sampling their parameters from a uniform distribution. The range of the distributions was determined either by the constraints and symmetries of the Gabor function (window and wave-generation function orientation), the patch sizes and resolution (horizontal and vertical position, intensity scaling, and frequency maxima), or the range of parameters produced by fitting Gabor components on the ICA components (window size and frequency minima). The Gabor functions generated by this method were rendered in 400 image patches that were 25×25 pixels and supplied as input to the fitting process described earlier in the same manner as a set of ICA components. The parameters of the fitted components were compared to the parameters of the Gabor functions that generated the image patch. Results of this comparison can be seen in Table 1. The distributions of the errors are highly nonnormal, with most of the parameter errors close to zero (see the column labeled “Median absolute deviation” [MAD]). However, a minority exhibit large outliers that drive larger mean squared errors. In most cases, both the MAD and the mean squared errors are less than the unit of measurement (e.g., pixels). The only exception is the window sizes, which have a mean squared error of 6.4 and 6.25 pixels. Even here, half of all errors are below 0.20 and 0.23 pixels. For the measures we are principally interested in—i.e., phase, frequency, orientation, and position—the error values are extremely low and less than the sampling rate of the image (i.e., less than one pixel), although the much larger values for mean squared error indicate the presence of large outliers. We conclude that the fitting method produces a generally accurate reflection of the true value of the underlying Gabor functions.

Parameter	Unit	Range	Median absolute deviation	Mean squared error
Horizontal Gabor center h	Pixels	[0, 25*]	0.0014	0.1052
Vertical Gabor centre v	Pixels	[0, 25*]	0.0013	0.1512
Window width σ_w	Pixels	[4, 12.5] [†]	0.2014	6.4004
Window height σ_h	Pixels	[4, 12.5] [†]	0.2271	6.2531
Window orientation ψ	Radians	[0, π]	<0.0001	0.2658
Wave-generating function frequency f	Cycles per pixel	[0.1 [‡] , 0.5 [‡]]	<0.0001	0.0006
Wave-generating function phase ϕ	Radians	$[-\pi, \pi]$	0.0012	0.1083
Wave-generating function orientation θ	Radians	[0, π]	<0.0001	0.2658
Scaling factor s	Intensity	[0.1, 1.0] [†]	<0.0001	0.2221

Table 1. Estimates of the accuracy of fitting of Gabor functions. Each parameter of the randomly generated Gabor function is sampled from a uniform distribution of the ranges shown. Unless marked, the ranges chosen are constraints of the Gabor functions. *Notes:* *The size of the image patch is 25 pixels. [†]At least 95% of fitted Gabors generated from the ICA model are between these values. [‡]The Nyquist limit is 0.5 c/pixel; wavelengths shorter than this cannot be detected.

log-Gabor functions

Although most studies of V1 (Prince, Cumming, & Parker, 2002) have fitted Gabor functions to response data, it has been suggested that log-Gabor functions are a more accurate fit to observed data (Field, 1987). In the context of binocular stereopsis, it has also been shown that an energy model based on log-Gabor functions can be developed, and would lead to more accurate estimation of binocular disparity (Faria, Batista, & Araújo, 2013). Unlike the standard Gabor function, log-Gabor functions are defined in Fourier frequency space rather than the image space. log-Gabor functions were defined in the polar Fourier domain as

$$LG(f, \theta | \theta_0, \theta_\sigma, f_0, f_\sigma) = \exp\left(-\frac{(\theta - \theta_0)^2}{2\theta_\sigma^2}\right) \exp\left(-\frac{\left(\ln\frac{f}{f_0}\right)^2}{2\left(\ln\frac{f_\sigma}{f_0}\right)^2}\right). \quad (7)$$

where f is the radius (frequency) and θ is the angle of the polar coordinates. The symbols f_0 and f_σ are, respectively, the principal frequency and the bandwidth of the frequency component (Fischer et al. 2007); θ_0 is the principal orientation; and θ_σ is the orientation bandwidth. log-Gabor functions have some significant advantages over standard Gabor functions. The responses of Gabor functions depend on the mean luminance of the stimulus, whereas the responses of log-Gabor functions do not. log-Gabor functions also have a long tail in frequency space, which more closely matches observations in primates (Hawken & Parker, 1987). However, for this study log-Gabor functions have two significant disadvantages. Firstly, most studies which have carried out physiological measurements have fitted Gabor functions to the data, making log-Gabor functions less directly comparable to these data and to the standard binocular energy model. Secondly, log-Gabor functions do not possess a windowing function with a clearly defined center as a

standard Gabor function does, rendering the analysis of position disparity more complex.

Parameters for Equation 7 were determined for ICA components by fitting a log-Gabor function in a similar manner to fitting a Gabor component. First, the ICA component was converted to Fourier space; then the mean squared error between the absolute value of the ICA component in Fourier space and the log-Gabor function was minimized using MATLAB's `fminsearch` function, initialized by a genetic algorithm (as described earlier in Fitting Gabor functions). We did not evaluate the accuracy of the log-Gabor fitting in as much detail as the Gabor fitting, but we found the algorithm to be extremely consistent. We fitted 400 test Gabor functions (see Fitting Gabor functions) 10 times with log-Gabor functions using `fminsearch` and the genetic algorithm with random initialization. The MAD of the deviations divided by the median of the deviations of the fitting error was used to determine the consistency of the fit. A high value would indicate an inconsistent algorithm. The values were divided by the median of the fitting error to prevent large fitting errors dominating the statistic. Over the 400 test Gabor functions, the mean of the MAD was 0.005. This indicates that the fitting algorithm is consistent and we can be confident that the error values it produces when fitted to ICA components are reliable.

In order to compare the accuracy of Gabor functions to log-Gabor functions as a description of the learned components of the ICA model, we first fitted both Gabor functions and log-Gabor functions to 8,000 components generated by the ICA model (4,000 left and 4,000 right view components). The accuracy of the fit was determined by measuring the mean squared difference between the fitted Gabor (or log-Gabor) function and the original component. As log-Gabor components are only defined in Fourier space, the ICA components and Gabor components were transformed to Fourier space and the mean squared difference calculated on the absolute values of the Fourier

components. This provided a measure of the accuracy of fit of the envelope only; phase is lost in this comparison. For 8,000 components (chosen randomly from the full set to reduce computation times), 7,897 were successfully fitted with both Gabor and log-Gabor functions.

The fitting error between the learned components and the Gabor functions and the fitting errors between the learned components and the log-Gabor functions were highly correlated (Spearman's ρ was 0.99986). Differences between the two measures were standardized by dividing by the mean of both log-Gabor and Gabor errors, and thus differences are specified in terms of overall fitting error. The median difference between the Gabor and log-Gabor error measurements was 0.003. This is less than the estimated level of consistency in the fitting (0.005, see previously). Of the fitted components, 43.7% exhibited standardized differences in error of less than the estimated level of consistency. For 37.3% of fitted components, the Gabor function was slightly more accurate than the log-Gabor function (median standardized error = 0.015), and for 19.0% the log-Gabor functions were slightly more accurate than the Gabor functions (median standardized error = 0.054). We concluded that log-Gabor functions were equally capable of describing the ICA components as were Gabor functions; however, they are unable to describe the position of the receptive field—which is important in our analysis—without an additional fitting stage in the spatial domain.

Bootstrapping

The accuracy of the fitting is only one source of error in the process. The computation of the ICA components depends on both the locations of the patches chosen (uniform random distribution across the image) and the initial starting point of the FastICA algorithm (random normal distribution with mean 0; Hyvärinen, 1999).

We used a simple bootstrapping method to generate new sample sets from the fitted Gabor functions. To generate a bootstrapped sample set, whole Gabor functions were sampled uniformly at random from the 40,000 fitted Gabor functions with replacement. In this fashion, 200 sample sets of 40,000 Gabor functions were generated. In order to calculate a distribution from the data—e.g., the distribution of phase disparities—a separate histogram was calculated for each of the bootstrapped sample sets. Identical bins were used for each histogram. We computed 95% confidence intervals (CIs) separately for each bin by sorting the data and taking the values of the 2.5 and 97.5 percentiles, respectively. These CIs can be seen as the

vertical bars on the histograms. For singular values, bootstrapped CIs are calculated in a similar manner: The statistical value is calculated separately for each of the bootstrapped sample sets and 2.5% and 97.5% CIs calculated from the 2.5 and 97.5 percentiles. Results of the bootstrapping analysis will be shown where appropriate for each of the distributions analyzed; generally this is restricted to histograms rather than scatter plots, as the CI of individual points cannot be computed by this method.

Properties of the ICA components

A detailed analysis was carried out on the parameters of the fitted Gabor functions on each of the 40,000 ICA components.

Degree of binocularity

Although the samples are left/right normalized to account for local illumination differences, there is no guarantee that the components generated from the ICA algorithm will contain binocular features. Monocular features—i.e., components with weak or nonexistent signals from one or the other view—will be generated when features in one view occur independently from features in the other view. A measure analogous to ocular dominance can be calculated from the ratio of intensity (s in Equation 5) between left and right component pairs. The larger of the two values was chosen as the denominator. The resulting ratio is directionless, with a ratio of 1 being a binocular component equally weighted in each eye and a ratio of 0 being a fully monocular component with no input from the contralateral eye.

From Figure 2A and B we can see that a bimodal distribution of luminance ratios emerges. The larger of the two groups peaks at 1 and indicates a set of binocularly tuned components. Of the components, 75% have a binocular ratio greater than 0.5. This is a conservative estimate, as 72% of components have a binocular ratio greater than 0.8. The smaller group that we designate monocular contains 25% of the components. Members of the monocular group have ratios less than 0.5. Again, this is a conservative estimate, as 24% have binocular ratios less than 0.2. A clear majority of components produced by the ICA show binocular tuned features, with little difference in intensity between left and right components. To test whether the binocularity evident in the majority of components truly reflects the interocular redundancies in the test images, luminance ratios were also computed for 4,000 ICA components trained on unrelated samples, drawn independently from the left and right images. Figure 2C and D shows the luminance ratios

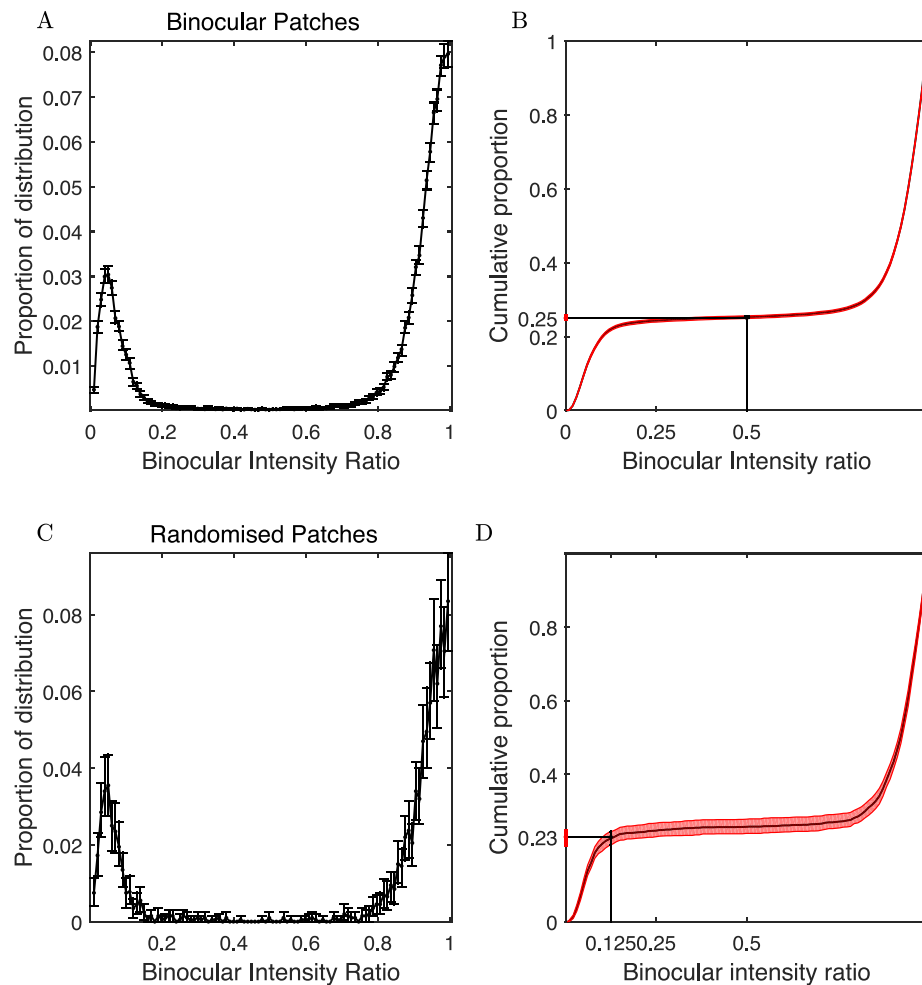


Figure 2. Ratio of intensities between left and right pairs of components. (A) A bootstrapped histogram of intensity ratios from 39,998 component pairs; 95% CIs are shown as black error bars. (B) The cumulative distribution of these ratios. The median of the cumulative distribution for each histogram bin is shown as a black line; the range covered by the 95% CIs is shown in red. The distribution is bimodal, with the bulk of intensities ranged towards left/right equality of intensity (i.e., 1). From (B) we can see that 75% of component pairs have ratios greater than 0.5. By way of contrast, (C) and (D) show the intensity ratios of ICA components trained on randomized patch pairs. (C) The distribution of random patch ratios as a histogram; 98% of the components have a ratio less than 0.125 (D).

for components trained on randomized patch pairs. Most components (98%) have a luminance ratio less than 0.125; the proportion of components with a ratio of at least 0.5 was not measurable with any estimate of accuracy (2 out of 4,000). The presence of binocular components in randomized patch pairs was negligible, so we are able to conclude that binocular components are generated by a relationship between the interocular signals.

Orientation and frequency analysis of individual components

Figure 3 shows the basic results of fitting Gabor functions to the generated components. A 2-D histogram of the locations of the centers of the Gabor

functions fitted to both left and right eyes can be seen in Figure 3A. The area of the heat map corresponds to the dimensions (in arc minutes) of the image patches, and the cells are colored according to the count of Gabor functions with centers in each cell. A clear boundary effect can be seen in the figure, with a large proportion of cells having a position at or close to 0 on either the x- or y-axis; this is an effect of the constraints on the fitting function. Away from the boundary area the full range of available possible positions is represented, with negligible clustering.

The distribution of window sizes can be seen in Figure 3B as a 2-D histogram (heat map) of window width σ_w against window height σ_h in terms of cycles in the wave-generating function. As the windows are rotated by ψ , the values of σ_w and σ_h do not conform to the x- and y-axes; the rotation is also independent of

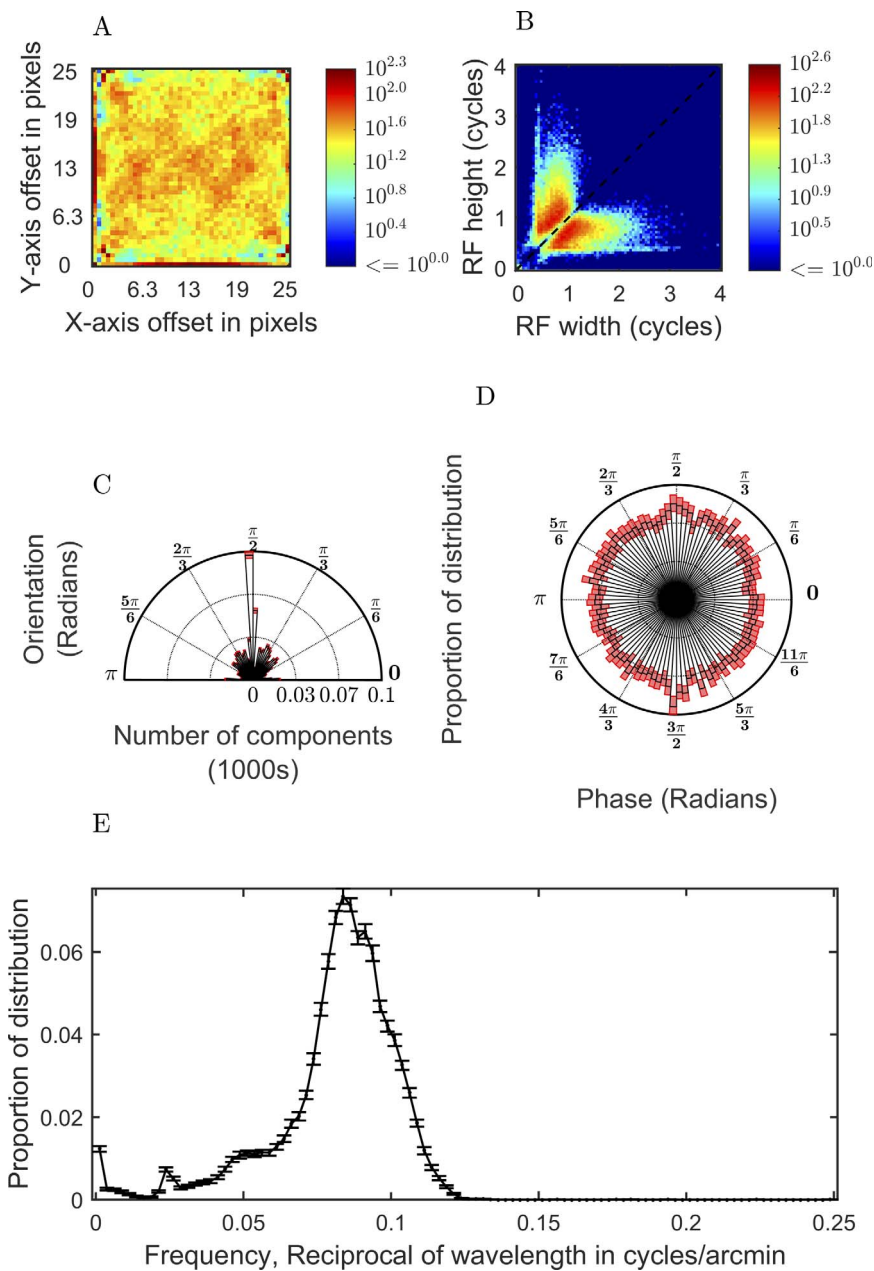


Figure 3. Results of fitting Gabor functions to the components generated from successive ICA of image patches. (A) A (log 10) heat map of locations of the Gabor functions, as measured from the center point of the windowing function. The boundary effect can be seen as a prevalence of high cell counts (red) along the $x = 0$ and $y = 0$ lines. (B) The distribution of two radii of the windowing function. There is a general tendency towards slightly elliptical functions. (C) A bootstrapped rose histogram of the wave-generating function's orientation. The values on the radius axis are histogram counts in thousands. A significant bias towards $\pi/2$ and 0 radians can be seen. (D) A bootstrapped rose histogram of the phases of the fitted Gabor functions. The values on the radius axis are histogram counts in thousands. The plot shows a generally even distribution of phases. (E) The bootstrapped histogram of frequencies of both left and right Gabor functions combined. The frequencies are $1/\text{wavelength}$ in arc minutes. The frequencies of the filters are highly clustered, most likely a result of the windowing effect of constraining the data to the size of the image patches. This issue is addressed in detail in the Scale subsection.

the rotation θ of the wave-generating function. The windows are biased towards oval shapes—few show circular shapes (shown on the graph as the dashed black line)—but these ovals are not generally particularly elongated. Measuring the window size in terms of

cycles also provides a useful indication of the bandwidth of frequency and orientation tuning (Ringach, 2002); a low value for the window size results in a broadband frequency-tuned component and a high value results in a narrowband frequency-tuned com-

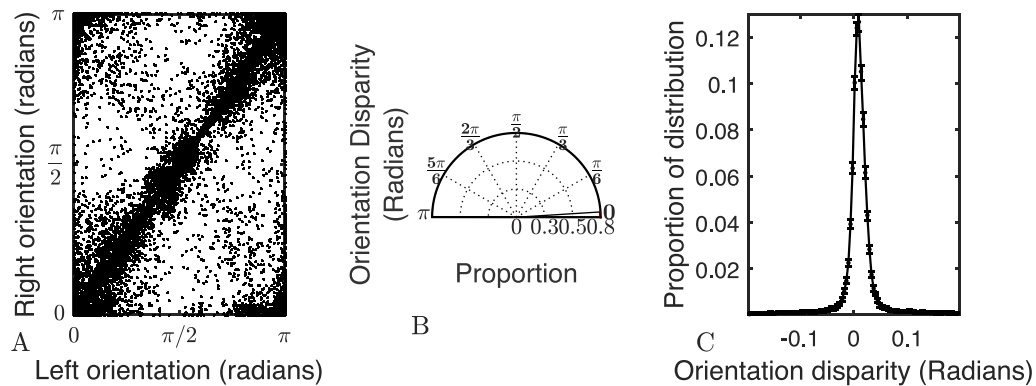


Figure 4. Comparisons of frequency and orientation between left/right pairs of Gabor functions fitted to ICA components. (A) The relationship between the orientations of the left and right parts of the components. (B) A bootstrapped rose histogram of the absolute angle differences between left and right fitted Gabors. (C) A scaled-up subset of the angle differences between $\pm\pi/16$. The main black line shows the median bootstrapped distribution, with the error bars showing the 95% CIs. Most fits produce Gabor functions with similar orientations.

ponent. Similar logic obtains for orientation tuning. The results show a strong tendency towards narrow-band tuning, with values for the standard deviation of window size generally greater than 1 in one of the principal directions (either σ_w or σ_h) and generally around 0.5 in the other. As noted by Ringach (2002), this is a substantial deviation from physiology, as most cells observed in the V1 area of the macaque visual cortex have window sizes of less than 1 and are therefore much more broadly tuned in frequency and orientation than the components learned using ICA. The median frequency bandwidth of the components was 0.675 octaves (95% CI [0.673, 0.677]). The median frequency bandwidth for cells in the visual cortex of the macaque is higher than this, around 1.4 octaves (DeValois, Albrecht, & Thorell, 1982). It is worth noting, however, that as the image patches were preprocessed using PCA—which is also a bandwidth-limiting process—the narrowband tuning of the learned components is likely to be a result of band-pass filtering in the preprocessing stage.

A bootstrapped rose histogram of the wave-generation function orientations θ is shown in Figure 3C. The black lines show the median of the distributions, with the 95% CIs shown as red bars. The orientations cover the range of possible values (0° to 180°), with a strong bias towards 90° and 0° (180° is equivalent to 0°). Although the distribution of edges in natural images is biased towards 0° and 90° (Hansen & Essock, 2004), it has been observed that ICA tends to produce results in which the orientation and frequency are aligned with the sampling grid (van der Schaaf & van Hateren, 1996). Consequently, we are not able to determine the extent to which these results are due to the prevalence of horizontal and vertical features in the binocular natural images or due to biases in the ICA algorithm.

The distribution of the phases ϕ of the fitted Gabor functions is shown in Figure 3D. Again, the medians of the distributions are shown as black lines and the 95% CIs in red. The distributions show a generally uniform distribution of phases.

The distribution of frequencies, in cycles per arc minute, is plotted as a histogram in Figure 3E. The error bars show the 95% CIs. The range of frequencies is constrained by the minimum wavelength detectable from the sampling lattice to be less than the Nyquist limit (0.5 c/pixel, 0.125 c/arcmin) and greater than or equal to 0 c/pixel (Shannon, 1949). A strong peak can be seen at 0.085 c/arcmin (5.1°). The distribution of frequencies is strongly influenced by the range of frequencies in the training image sets and the implementation of the ICA algorithm (van Hateren & van der Schaaf, 1998). Although the Nyquist limit is 0.125 c/arcmin, this requires that the wave-generating function be perfectly aligned with the sampling lattice, and thus the limit is lower in practice. The size of the windowing function is also a factor, as there are more ways to pack smaller Gabor functions into the space of the sample image while maintaining the independence of the samples.

Disparity analysis

Frequency- and orientation-disparity analysis

Figure 4A shows a scatter plot of left-view orientation against right-view orientation. The difference in orientation is shown in Figure 4B and C. There is a clear peak around 0, showing that most interocular differences in receptive-field orientation are small. Components are present across the whole range of orientation differences but clustered around 0. The left and right orientations are extremely highly correlated: Pearson's $r^2 = 0.99$, 95% CI [0.993, 0.993], $p < 0.001$,

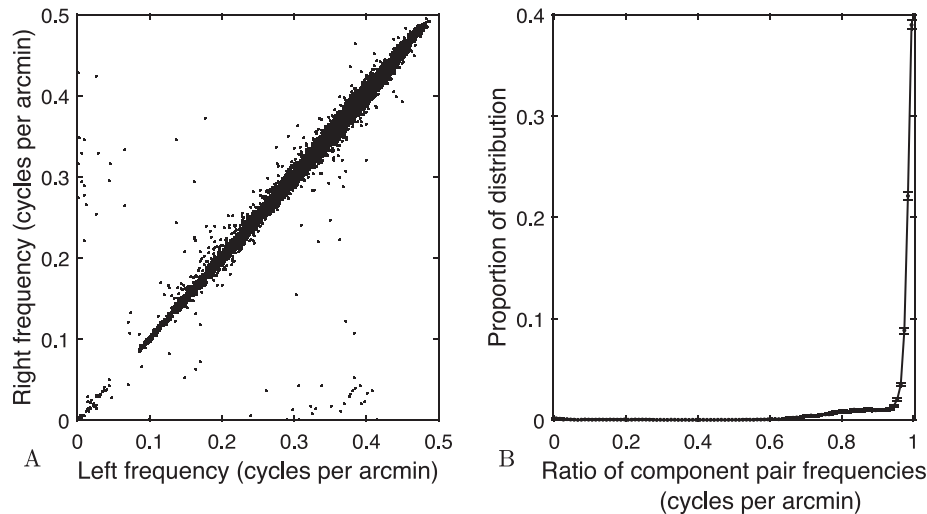


Figure 5. Distribution of tuning frequencies of binocular Gabor pairs. (A) The distribution of pairs as a scatter plot. A clear linear relationship is visible between left and right frequencies. (B) The bootstrapped histogram of left/right frequency ratios. For consistency, ratios greater than 1 have been inverted to ensure a smallest/largest ratio. Most components have a frequency difference close to 0. The main black line shows the median bootstrapped distribution, with the error bars showing the 95% CIs.

95% CI [<0.001 , <0.001]. The spread (median of absolute deviation) of orientation disparities is 0.0196 radians, 95% CI [0.02025, 0.02024]; the standard deviation is 0.086 radians, 95% CI [0.08122, 0.09395].

Figure 5 shows the relationship between left and right frequencies for the fitted functions. Again there is a clear linear correlation between left/right frequencies Pearson's $r^2 = 0.98$, 95% CI [0.982, 0.984], $p \leq 0.001$, 95% CI [<0.001 , <0.001]. As before, a minority of components do not fit the linear profile and thus appear as outliers in the plot. The vast majority of components are tuned to the same frequency in each view (see Figure 5B).

Phase-disparity analysis

Given twin left/right Gabor responses, two forms of disparity can be calculated: phase disparity and position disparity. A position disparity is a shift in the location of an otherwise identical receptive field between the two views. In contrast, a phase disparity is a change in the shape of the filter, in the form of a shift in the Gabor phase component. This shift is orthogonal to the direction of the component's orientation by definition. Using the phase information from the Gabor functions fitted to the ICA components, we calculated the phase difference as the shortest distance around a circle from the two angular phase positions. The distributions of the observed phase differences can be seen in Figure 6, as a polar histogram in Figure 6A and a standard bar histogram constrained to the range $[0, \pi]$ in Figure 6B. The plots show a strongly bimodal distribution of phase disparity, with peaks at 0 and π radians and troughs at $\pi/2$. The distribution is also

asymmetric with a bias toward π phase components, indicating a bias in the ICA results towards antiphase components.

Position-disparity analysis

The Gabor functions consist of two parts, a sinusoid and a windowing function. For each ICA component, the center of the windowing function is found for the left and right parts of the component separately. The displacement disparity between left and right Gabor functions is measured as the distance between the centers of the windowing functions. This can be measured in the horizontal and vertical directions or in the directions parallel and orthogonal to the orientation of the filter. We consider both.

Simple vertical and horizontal disparities can be calculated by subtracting the left-view position coordinates from the right-view position coordinates ($h_r - h_l$, and $v_r - v_l$). Figure 7 shows the marginal distributions of the horizontal and vertical disparities, respectively. For horizontal disparities, negative values indicate components tuned to detect near disparities, and positive values indicate components tuned to detect far disparities. For vertical disparities, positive values indicate that the receptive field is shifted upward in the right eye compared to the left eye, and negative values indicate the reverse. As the distributions had very long tails, the plots only show data between the 1.25 and 98.75 percentiles. The distributions were calculated using 100-bin histograms and CIs calculated using 200 bootstraps.

The distributions of both horizontal and vertical disparities are highly peaked and roughly symmetric

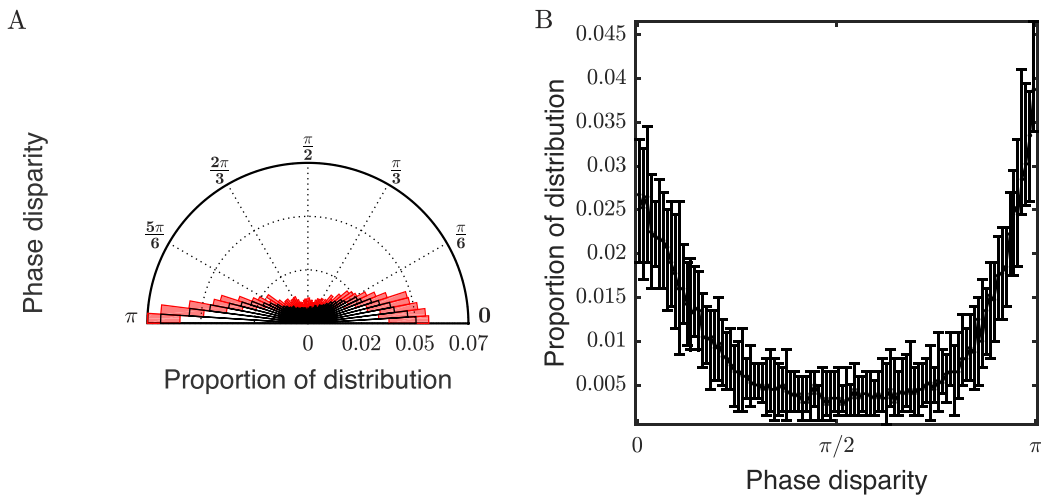


Figure 6. Distribution of absolute phase disparity in the components. In a polar histogram of the angular distance between left and right phases (A), the black boxes show the median of the bootstrapped distribution for each angular cell and the red boxes show the 95% CI for each cell. (B) The bootstrapped histogram plot of the same results with 95% CI shown as black bars. A bimodal distribution can be clearly seen in the two plots, with the difference between peak and trough that is clearly larger than the estimated error in the distribution. The distribution of binocular phase differences are clearly asymmetric (about $\pi/2$), with a significant difference between the 0 and π phase components.

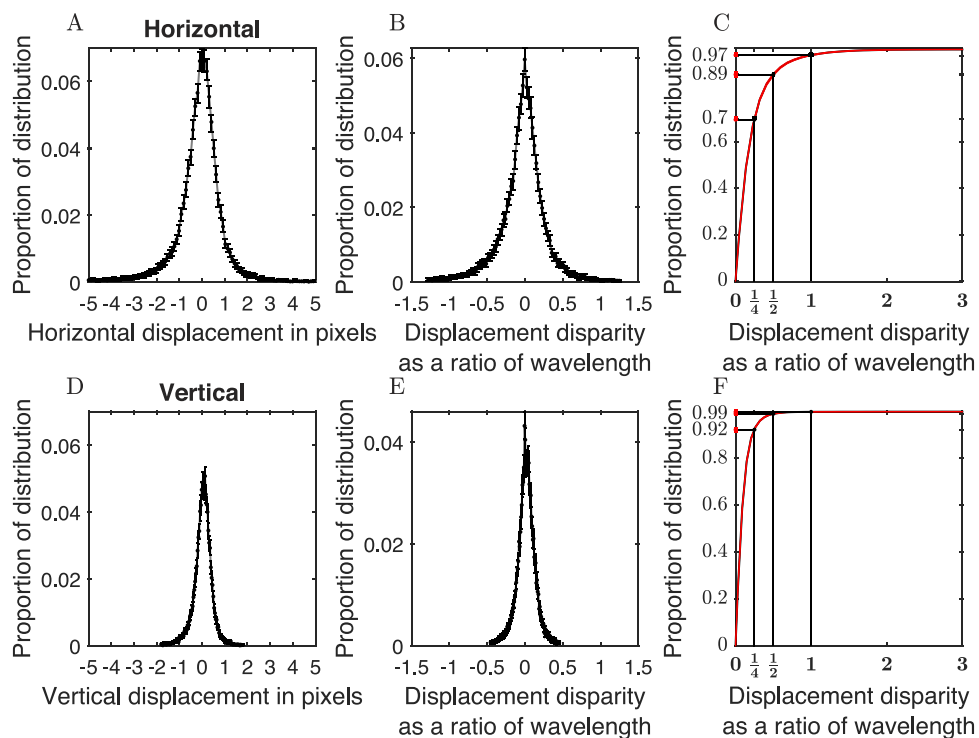


Figure 7. (A, D) Marginal distributions of the horizontal and vertical disparities between left and right view fitted Gabor functions, computed as bootstrapped histograms with 100 bins. The distributions are limited to 98.25% double-sided quintiles. The distributions are clearly peaked at 0, broadly symmetric, and highly kurtotic. (B, E) The displacements as a function of the frequencies of the fitted functions. (C, F) The cumulative distributions of the horizontal and vertical displacements, respectively. The median of the computed distributions is shown as a black line, and the 95% CIs are shown in red. The proportions of the distributions with disparities of less than 0.25, 0.5, and 1 cycle are marked, along with the CIs of proportions, shown as red lines on the vertical axis.

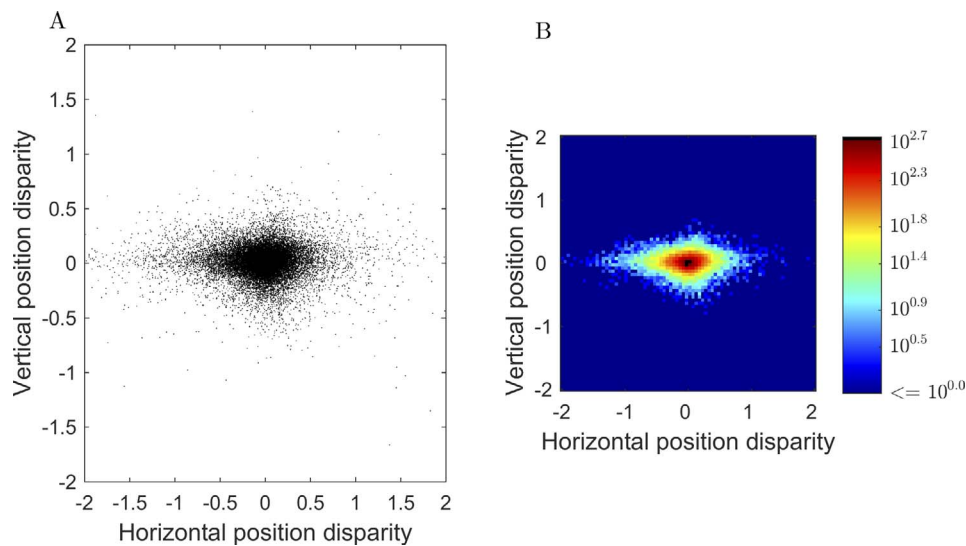


Figure 8. The joint distributions of the horizontal and vertical position disparities as a ratio of wavelength. (A) A scatter plot of all the computed locations (27,661 in total). (B) A 2-D heat map of the distribution with each cell color-coded to show the log of the cell count.

about 0, indicating an even mix of near- and far-tuned features, and appear to obey a double-sided power law. As can be seen in Figure 7A and D, the majority of displacements are less than 1 pixel. These small displacements are likely to represent true disparities rather than chance fluctuations, since the medians of the absolute position-disparity distributions—0.39 pixels, 95% CI [0.390, 0.402], for horizontal disparity and 0.20 pixels, 95% CI [0.198, 0.194], for vertical disparity—are much greater than the MAD estimated when the accuracy of the fitting was analyzed (0.0028 and 0.0026, respectively). The 95% CIs show the range of the bootstrapped distributions. As the cameras, mimicking our eyes, are separated horizontally, we would expect a wider range of displacements on the horizontal axis compared to the vertical axis. The standard deviation of the horizontal displacements was 0.94 pixels, 95% CI [0.924, 0.948], and for the vertical displacements was 0.42 pixels, 95% CI [0.413, 0.422]. These nonoverlapping values match expectations that the distribution of horizontal disparities is broader than that of vertical disparities. Both horizontal and vertical position-disparity distributions had similar excess kurtosis. The bootstrapped kurtosis is 3.52, 95% CI [3.384, 3.731], for the horizontal distribution and 3.70, 95% CI [3.536, 3.891], for the vertical distribution. An excess kurtosis of 3 indicates that the distribution of both horizontal and vertical position disparity follows a double-sided Laplacian. The first and last half percentiles of each distribution were rejected as outliers in this analysis.

Figure 7A and D shows the distributions of position disparity in pixels. These are replotted in Figure 7B and E to show disparities as a ratio of the wavelengths of

the individual components. The corresponding cumulative distributions are plotted in Figure 7C and F. From these, we can see that 89.1%, 95% CI [88.64%, 89.42%], of horizontal and 99.1%, 95% CI [98.90%, 99.17%], of vertical position disparities are less than half a cycle.

The joint distributions of horizontal and vertical disparities are plotted in Figure 8. Horizontal and vertical disparities are uncorrelated—Pearson's $r = 0.028$, $p < 0.001$, $n = 37,028$ —and the mutual information is low (0.0846, calculated using a 2-D histogram with 1,098 bins using base 2), indicating that the distributions are independent.

An alternative way to describe the distribution of two-dimensional disparities is in terms of the magnitudes of disparity in directions parallel and orthogonal to the orientation tuning of the filters. Analyzing disparity in this way is of interest since previous work has assessed the extent to which the direction of disparity to which neurons are tuned is related to their orientation tuning (Cumming, 2002; Gonzalez, Justo, Bermudez, & Perez, 2003; Read & Cumming, 2004b). The distributions of disparities are plotted in this way in Figure 9. As before, we cut the long-tailed distributions at the 98.25 percentile and generated confidence intervals using 200 bootstraps. Again, the distributions are clustered about 0, with an exponentially decreasing proportion of components as disparity increases. As can be seen in Figure 9B, the vast majority of components—98.0%, 95% CI [97.75%, 98.57%], in the orthogonal direction and 90.0%, 95% CI [89.38%, 90.01%], in the parallel direction—have disparities of less than half of the wavelength. The excess kurtosis is 3.04, 95% CI [2.915, 3.156], for

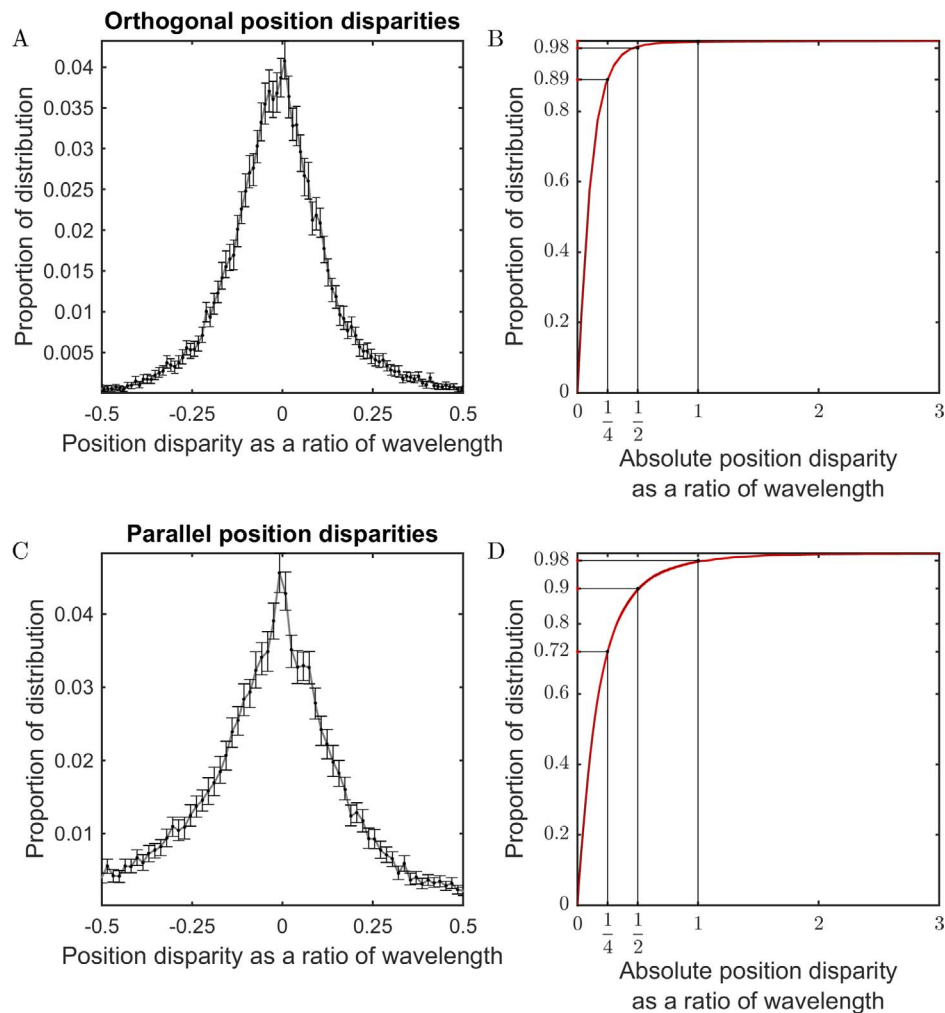


Figure 9. Distributions of position disparities as a ratio of wavelength. (A, C) Bootstrapped histograms of position disparities oriented (A) orthogonal to and (C) parallel to the Gabor orientation. (B, D) The bootstrapped cumulative distributions for (A) and (C), respectively. All distances are ratios of the component wavelength. Positive disparities indicate components tuned to detect far-type disparities, negative disparities indicate components tuned to detect near-type disparities.

components in the direction orthogonal to the orientation tuning and 1.52, 95% CI [1.434, 1.576], in the parallel direction.

Next, we directly compared the direction of positional disparity with the orientation tuning of the components. The direction was calculated as the inverse tangent (atan2) of the vector between left and right Gabor centers. This angle thus determines the direction of positional displacement in an image-based (horizontal/vertical) rather than component-based (parallel/orthogonal) coordinate system. Figure 10A shows a rose plot of the bootstrapped distribution of disparity directions independent of the components' orientation. The distribution is clearly biased towards horizontal (Hodges–Ajne test $p < 0.001$; Berens, 2009). Figure 10B shows a heat map of orientation of position disparity against orientation of the components. From the heat map, no clear association is visible between position-disparity orientation and orientation of the

filters; no correlation was found (using directional statistics) between position-disparity orientation and orientation of the filters, $p = 0.0863$, $c = -0.0111$ (Jammalamadaka & Sengupta, 2001, as implemented by Berens, 2009).

The relationship between position- and phase-disparity tuning

Figure 11 shows a scatter plot of phase disparity against position disparity. As the position disparities are long-tailed, the plot shows only disparities of less than 1 wavelength. This captures 97.7% of the components. The figure shows that the components span the full range of joint position and phase disparities. In the figure we can see the bimodal structure of the phase distribution as clusters around 0 and $\pm\pi$.

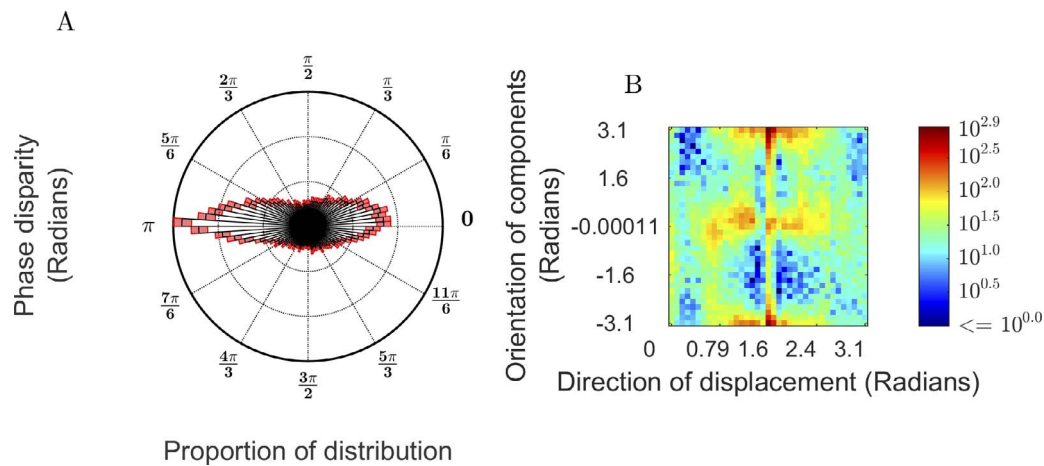


Figure 10. Distribution of direction of disparity. (A) A rose plot of the distribution of disparities between left and right fitted components. The black lines show the median counts in each bin, the red bars show the range of the 95% CIs of the bootstrapped distributions. An angle of 0 radians indicates a vertically oriented Gabor function, with positive angles indicating counterclockwise rotation. Similarly, a displacement angle of 0 radians indicates a vertically oriented displacement. A clear and consistent bias towards horizontal rather than vertical position disparities is also visible, with the distributions showing a smooth transition in between the horizontal and vertical directions. (B) A log 10 heat map showing the joint distribution of the orientation θ of the components against the direction of position disparity.

Phase and position disparity are related by the Fourier shift theory; thus, given a phase disparity, a similar position disparity can be calculated according to Equation 6. Part of the interaction between phase and frequency can be calculated by

$$d_c = (\hat{x}_r - \hat{x}_l) - \frac{(\phi_r - \phi_l)}{2\pi f} \quad (8)$$

Where \hat{x}_r and \hat{x}_l are the right and left component positions of the Gabor windows projected onto the wave-generation function's direction (see Equation 4); ϕ_r and ϕ_l are the phase of the left and right component Gabor functions; and d_c is effectively the difference in the underlying wave-generation function of both components. When measured in terms of wavelength ($d_c f$), an integer value (0, 1, etc.) indicates that the peaks and troughs of the wave-generating function of the left and right components align, such that the peaks and troughs fall in exactly the same locations in the receptive fields. A $d_c f$ of half-integer values indicates that the wave-generating function is anticorrelated, with the peaks in one eye aligning with the troughs in the other and vice versa. Note that in both cases the windowing function is free to move, so the components can have a different configuration of sidebands as the windowing function covers/uncovers different parts of the wave-generating function.

A plot of the distribution d_c for the fitted Gabor functions can be seen in Figure 12. Values of d_c are shown in terms of the both pixels and the wavelength of the individual fitted Gabor functions, and are strongly clustered around half-integer multiples of the wave-

length. This fits well with the strongly correlated and anticorrelated phase results just mentioned, as correlated components would be separated by integer multiples of the wavelength and anticorrelated results would be separated by wavelengths of an integer plus 0.5. By calculating the proportion of components contained within each half-wavelength band, we found that a substantial proportion of components—35.6%, 95% CI [34.86%, 36.16%]—are tuned to zero disparity. A larger proportion are tuned to anticorrelated components: 46.65%, 95% CI [45.38%, 47.59%] are in the combined ± 0.5 -wavelength categories.

The discrete nature of the combined disparity cannot be entirely explained by clustering of the position-disparity components around 0 (see Figure 9), as the combined disparities are peaked at more locations than 0 and the position-disparity function is much broader than the combined disparity clusters. Nor can it be explained entirely by clustering of phase disparity, although the 0- and π -radian phase disparities could account for the 0 and 1/2 combined disparity peaks—but again the distribution is too narrow. Instead, the effect is produced by the interaction of phase and disparity.

Scale

As shown in Figure 3E, the ICA components capture only a narrow range of frequencies. To widen the range of frequencies captured in their analysis, van Hateren and van der Schaaf (1998) varied the size of the patches

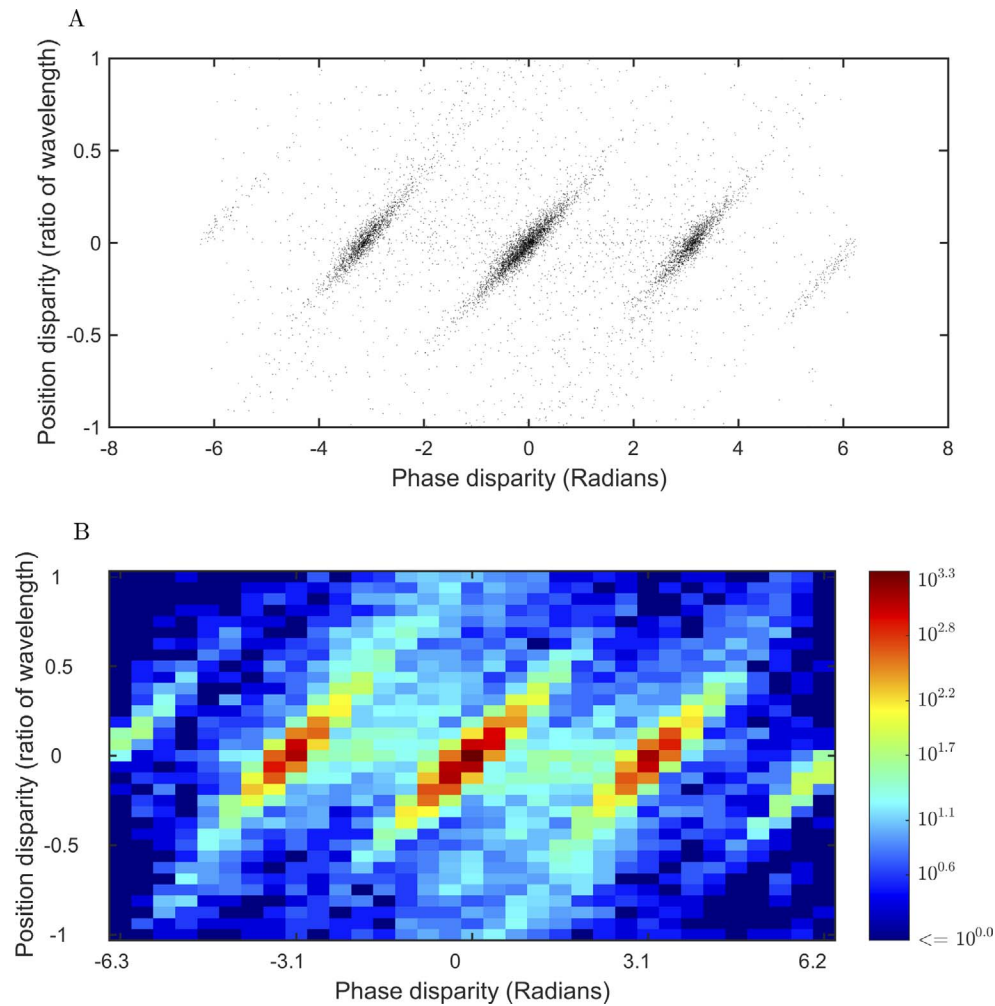


Figure 11. Phase displacement in radians against position disparity as a fraction of wavelength. The lines that appear suggest a link between phase and position disparity. The central cluster shows correlated binocular components; the left and right clusters show anticorrelated components.

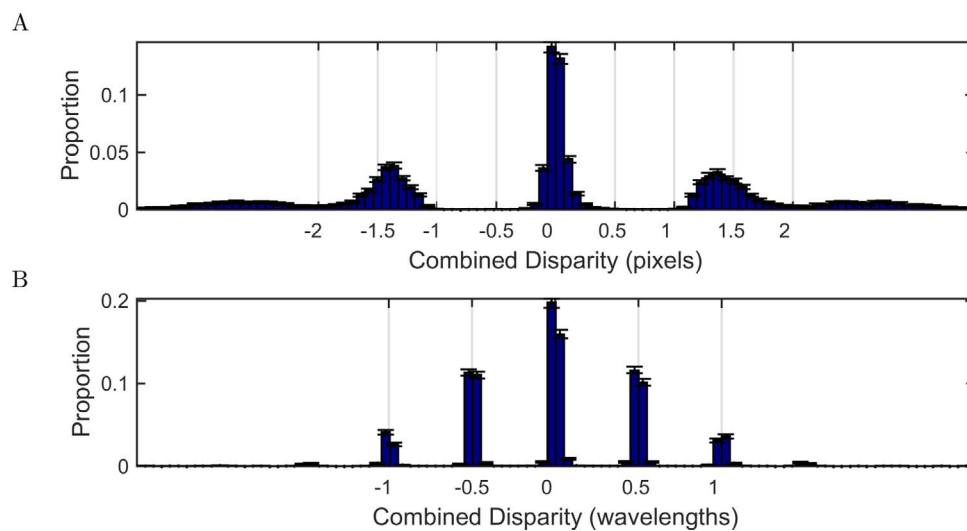


Figure 12. Distribution of combined disparity (disparity remaining when phase and position disparity are accounted for— d_c from Equation 7) for valid ICA components, calculated using 100 uniformly spaced bins; 95% CIs are shown as black error bars. The top plot shows the combined disparity measured in pixels, the bottom chart shows the combined disparity in terms of the wavelength of the individual filters.

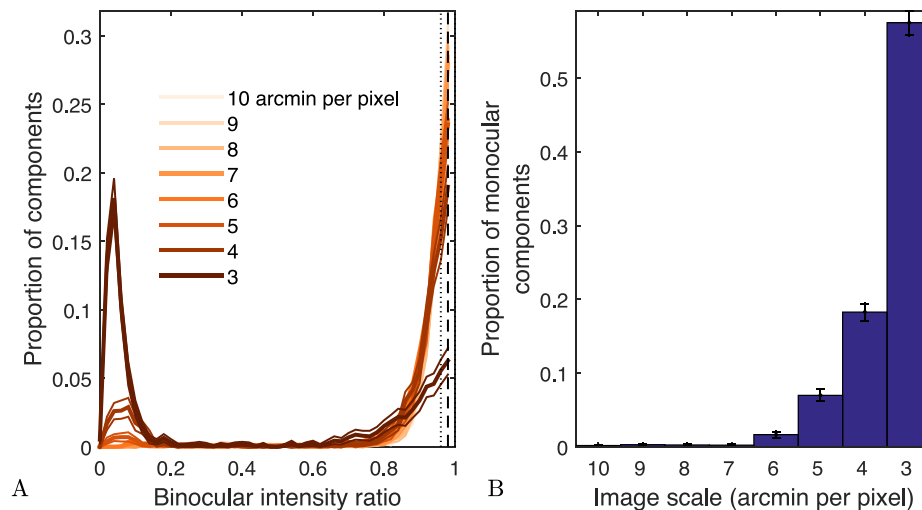


Figure 13. The effect of image scale of the proportion of monocular features. Images at the coarsest scale, 10/pixel, show the smallest proportion of monocular tuned components, and images at the finest scale show a high proportion of monocular tuned components. (A) The bootstrapped histograms of the intensity ratios at each scale. The median of the bootstrapped distribution is shown as a thick line, the 95% CIs are shown as thin lines. Fine scales show strong peaks at ratios close to 0 (monocular) and coarse scales show a bias towards a ratio of 1 (binocular). (B) The proportion of monocular components at each scale (in arc minutes per pixel). The blue bars show the median proportion of monocular components, the 95% CIs are shown by the black error bars.

sampled. Capturing the coarsest scales here would require image patches too large to feasibly compute using ICA. Thus, rather than vary the size of the image patches, we kept it constant at 25×25 pixels and rescaled the images. We chose 10 scales, each an octave apart, such that one pixel in the patches covered an area from 10×10 arcmin at the coarsest scale to 1×1 arcmin at the finest. Components were computed using ICA, and Gabor functions were fitted using the method already described. Distributions were calculated using 200-bin histograms with CIs calculated by bootstrapping using 2.5 and 97.5 percentiles to mark the 95% CIs.

The exact distribution of frequencies depends on both the ICA process and the frequency content of the images. To disambiguate the two we calculated the distributions of ICA components relative to two frames: the sampling grid—i.e., relative to pixels in the image patches—and the visual field of the images, measured in arc minutes. If the distributions are constrained by the sampling grid, they will be identical across scales when calculated in the sample-grid frame but differ in the visual-field frame (arc minutes). By contrast, if the sample grid has no effect on the ICA components' distributions, they will be identical across scales in the visual-field frame (arc minutes) but differ in the sample-grid frame. It should be noted that the effect we are discussing is a windowing effect—i.e., the components must exist within the image set in order to be detected. The sampling grid simply constrains our view of the data set.

Degree of binocularity across scales

As discussed earlier, not all components will contain binocularly tuned features. The proportion of monocularly tuned components will reflect the degree of independence between the left and right views. As the size of features detected is likely to vary across scale while the actual disparities remain constant, it is likely that the proportion of binocular components will change also. In particular, we would expect to find fine-scale features exhibiting a greater degree of independence between views as the disparities become greater than the wavelength.

We assessed the degree of binocularity using the same ratio of intensity as before. Figure 13B shows the proportion of monocular components generated for each of the 10 scales. Here a monocular component is defined as having a ratio of less than $1/19$ —i.e., more than 95% of the energy in the component is in the dominant eye. Coarse scales, those of 6 arcmin/pixel or more, show almost no monocular components, while the vast majority of components at the fine scale are monocular. While the distribution of actual disparities in the images is not known, it seems likely that the tendency toward monocular components at the finest scales is due to the disparities in the scene being larger than the features detected. Thus, coarse-scale feature detectors are better tuned to detect the disparities found in the image set.

As we are primarily interested in binocular disparity, we excluded monocular components from further analysis. Due to the small number of binocular components available from the finest two scales, we

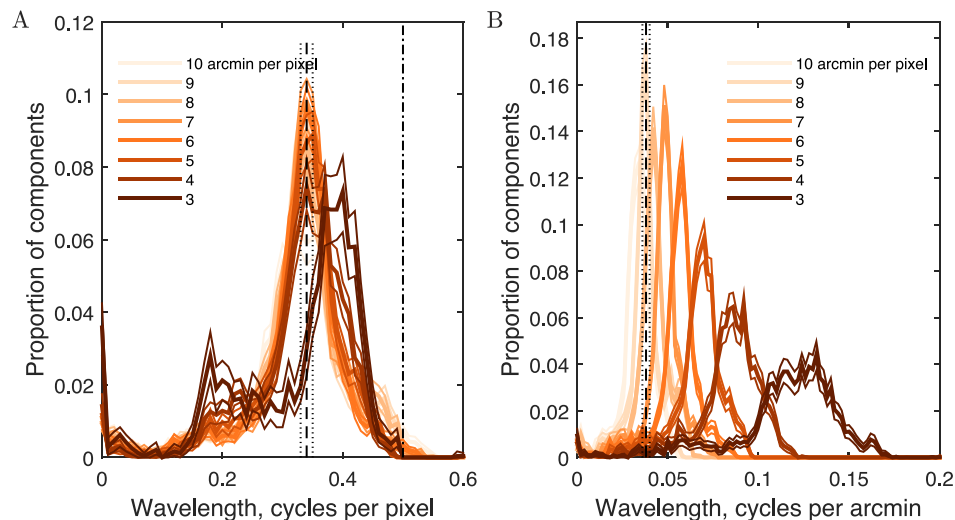


Figure 14. Results of ICA analysis at varying scales. The scales are measured in arc minutes per pixel. All plots show bootstrapped histograms with the median shown as a thick line and the 95% CIs shown as thin lines. The edges of two of the histogram bins are shown as dashed and dotted lines. (A) The distribution of frequencies in cycles per pixel for each of the 10 scales. The Nyquist limit is shown as a dot-dashed line. Most of the coarse-scaled frequencies show highly similar distributions, with some bias towards higher frequencies at the finest scales. (B) The same distributions as cycles per arc minute. At coarser scales, the tuning shifts to lower frequencies.

restricted further analysis to scales coarser than 3 arcmin/pixel.

Frequencies across scales

Figure 14 shows the distribution of frequencies for components learned across a range of scales. The distributions are plotted in two modes. In the first, the frequencies are measured in cycles per pixel; this shows the effects of the sampling grids and patch size on the frequencies. If the detected frequencies of the components depend principally on the size of the patch, we would expect the frequency envelopes to be identical or similar at all image scales. The second mode shows the frequencies rescaled to cycles per arc minute of visual angle and allows comparison with actual image features. For all but the finest scale, the distributions, measured in cycles per pixel, are almost identical (Figure 14A). The largest deviation is found in the 3-arcmin scale. Figure 14B shows the frequency distributions rescaled to show their true wavelengths in cycles per arc minute. The frequencies of the components cover a broad range from 0.02 to 0.16 c/arcmin (1.2–9.6 c/°). The full distribution is shown as a red line. The distributions are highly bandwidth limited due to patch and sampling-grid size. The number of components generated at each scale is fixed and only affected by the proportion of monocular components. It is clear that the resulting overall distributions of frequency tuning owe more to the ICA sampling method than to the distribution of frequencies in the image.

Position disparities across scales

The original image set contains a wide but unknown range of disparities that may not be adequately captured at the scale chosen in the detailed analysis presented earlier. Widening the scale will capture a wider range of disparities; however, as with frequency, the question of whether the distributions are affected by the ICA method remains. Again, we can test this by comparing the disparity distributions across scale and comparing them relative to the ICA sampling grid and to the original image dimensions. Figure 15 shows the distributions of position disparity across scales, both relative to the sampling grid (pixels) and relative to the visual field (arc minutes). The distributions are shown both in absolute terms (Figure 15A and B) and in horizontal (C and D) and vertical directions (E and F). Measured relative to the sampling grid, the position-disparity distributions show a trend towards more kurtotic (peaked) distributions at coarse scales compared to fine scales. The trend is most marked in the horizontal and vertical directions (Figure 15C and E). When measured in terms of the actual visual angle, this trend is reversed, with fine scales showing a more kurtotic distribution than coarse scales (Figure 15B and F), except in the horizontal direction, where no effect is visible. If the distributions are heavily biased by the ICA algorithm or sampling grid, we would expect highly similar distributions across scales.

The large variance in the distributions of position disparity in both the horizontal and vertical directions, when plotted in pixel units, suggests that the sampling grid alone is not driving the distribution. Similarly, if

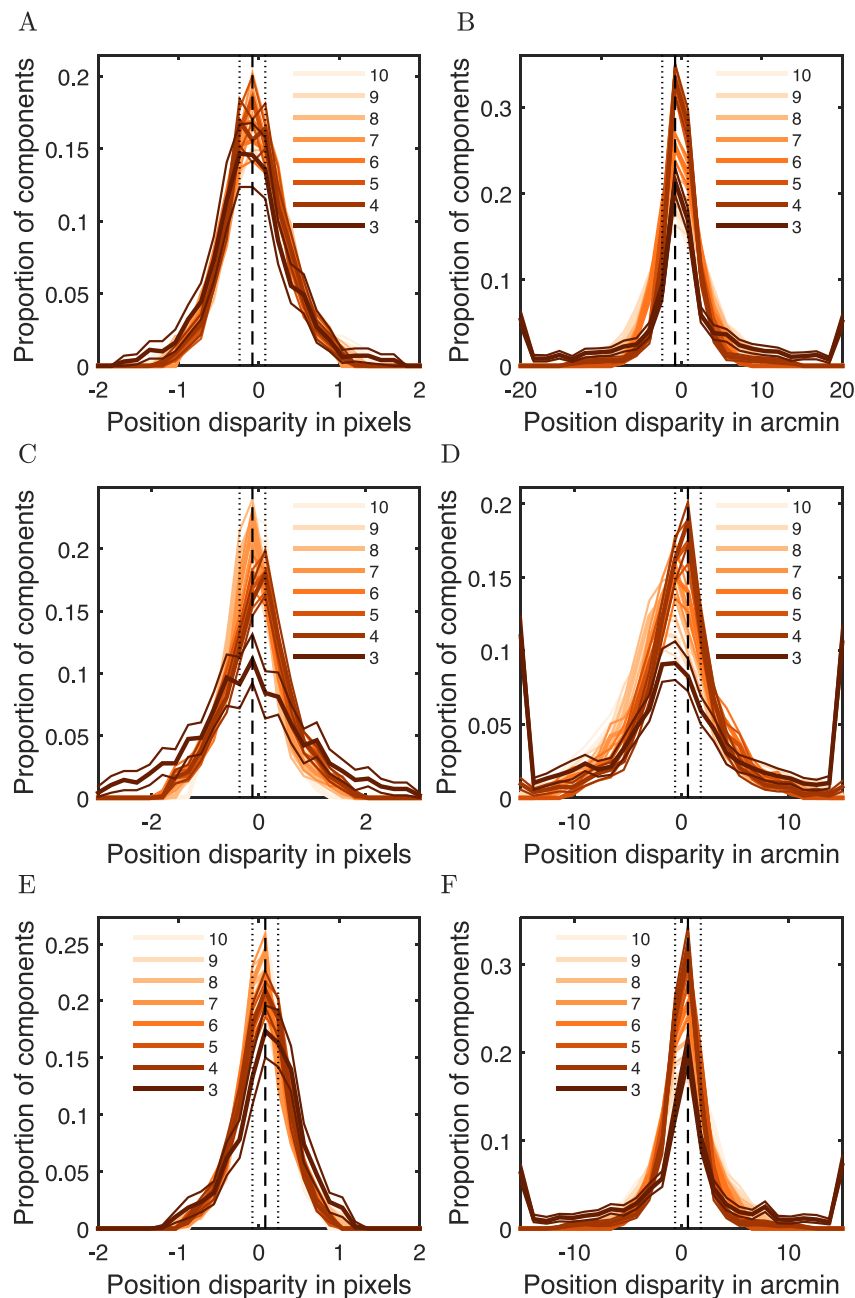


Figure 15. Comparison of disparity distributions across scales. Scales between 3 and 10 arcmin/pixel are shown as bootstrapped distributions of varying shades. As before, the thick lines denote the median of the distribution, thin lines the 95% CIs, and dotted and dashed lines the edges of histogram bins. (A, B) The distribution of absolute position disparities across the scales measured in pixels (A) and arc minutes (B). Fine scales show a strong bias towards small disparities, while coarse scales show a wider coverage. (C, D) The horizontal position disparities in pixels (C) and arc minutes (D). (E, F) The vertical position disparities in pixels (E) and arc minutes (F). As with the absolute displacements (A, B), fine scales shows a bias towards small disparities while coarse scales show a wider distribution; however, in the horizontal case it is weaker. Unlike the frequency distributions, which are strongly tied to the size of the patches, the position disparities vary across scales.

driven purely by the sampling grid, the range of position disparities, measured in arc minutes, would double when the sampling rate halved. While the range of position disparities in arc minutes is wider at coarse scales, the width does not double with a halving of the scale.

Phase disparities across scales

The distributions of phase disparity across scales can be seen in Figure 16. The distributions are highly similar across scales. This indicates that the results hold over a range of frequencies between ~ 2 and ~ 10 $c/^\circ$.

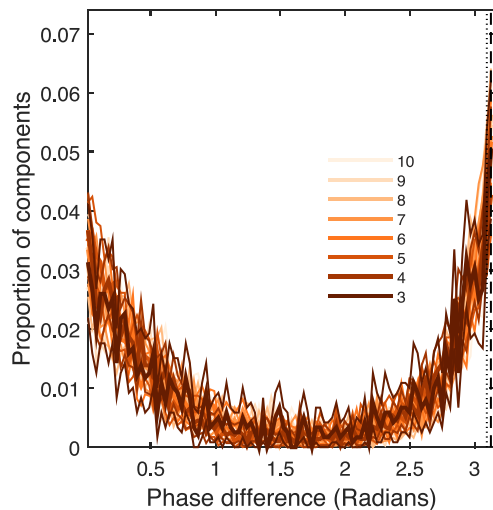


Figure 16. Bootstrapped distributions of phase differences across scales. The phase distributions follow the same bimodal pattern across the selected scales.

Relating the results to physiological findings

The ICA algorithm seeks to produce components that are maximally independent. In order to determine whether the resulting components provide an accurate model of binocular neurons, we directly compared the ICA components with physiological measurements. We describe the similarities in qualitative terms, paying close attention to similarities in the types of distributions and, where applicable, the ranges they cover.

Whitening

It has been hypothesized that whitening of image information is performed by center-surround cells in the retina (Atick & Redlich, 1992; Srinivasan et al., 1982). By analyzing the spatial tuning characteristics of P-cells in the retina (using data published by Croner & Kaplan, 1995), Graham, Chandler, and Field (2006) found that the sensitivity of P-cells is well matched to the power spectra of natural scenes. However, due to correlations that remained among neighboring P-cells, they came to the weaker conclusion that the P-cells performed an approximate response-spectrum flattening. In our work we used PCA, as it is a prerequisite of ICA; however, the spectral flattening performed in the retina provides some ecological validation for the PCA-based whitening step.

However, it should also be noted that the PCA components generated in our analysis do not resemble the center-surround responses found in retinal P-cells. The center-surround responses of these cells are limited to half-cycle representations, while the PCA components have multiple cycles, the number of which depends on the wavelength. This results in eigenvectors

(components used in the whitening) with a significantly larger receptive field than retinal ganglion cells. This may have implications for the receptive-field size of ICA components that will be discussed later.

Orientation- and spatial-frequency-disparity tuning

Gabor functions tuned to cover the full range of orientations were found in both left and right view parts of the components (see Figure 3C). However, actual orientations were closely clustered on 0 , $\pi/2$, and π , corresponding to the sampling grid. ICA has a tendency to produce components aligned with the sampling grid, as these have a lower energy state than unaligned states (van der Schaaf & van Hateren, 1996). It is known that a particular tendency for horizontal and vertical orientations exists in photographic images (Hansen & Essock, 2004). While this may well to some extent reflect an anisotropic distribution of orientations in nature, it is also likely to result from the alignment of structures with the cardinal directions when composing photographs (van Hateren & van der Schaaf, 1998). It is not possible to attribute the anisotropy in our results to any corresponding anisotropy in the natural environment, since it is likely to be driven to a large degree by the sampling grid in our photographs (van Hateren & van der Schaaf, 1998). The orientations of the left and right Gabor functions of the binocular-component pairs were highly correlated ($r^2 = 0.99$, $p \leq 0.001$). This is similar to results from physiology; Bridge & Cumming (2001) reported an almost identical correlation of $r^2 = 0.985$ and a spread (standard deviation) of orientation disparities of 9.22° . We observed a spread (standard deviation) of 3.55° , around half that of their result but of a similar order of magnitude. Due to the small angles involved, measurement noise could account for the discrepancy. This result supports the idea that a matching process, where features in one eye are matched with similarly oriented features in the other, is an efficient mechanism to code binocular scenes and therefore an effective strategy to compute binocular disparity.

The modal frequency of the components in the main analysis was ~ 4.8 $c/^\circ$ and ranged between ~ 0 and ~ 7 $c/^\circ$. This places the components within the range of frequency tuning of binocular simple cells in the macaque visual cortex (Prince, Pointon, et al., 2002). This indicates that the range of frequencies selected by the band-pass filtering in the whitening stage is appropriate for comparison to physiology. The frequency distribution is skewed towards higher frequencies (~ 4.8 $c/^\circ$); this resembles the results from physiology (see Prince, Pointon, et al., 2002, figure 4e).

Ringach (2002) noted a difference between receptive-field sizes computed for ICA components and those measured physiologically in both cats and monkeys,

specifically a substantially greater proportion of broadband-tuned cells compared to the tunings of ICA components. We found a similar effect in our data (see Figure 3); in fact, many of our ICA components are even more narrowly tuned than Ringach's. This indicates that a substantial number of V1 simple cells have a much smaller receptive field than measured here. A bias toward narrowband frequency-tuned components is a result of band-pass filtering in the PCA preprocessing stage. As discussed by Ringach et al. (1997), band-pass filtering will remove high-frequency information from the samples and subsequently from learned components; this can introduce ripple-like structures, which results in the components being biased towards narrow frequency bandwidth. As measurements of phase, frequency, and orientation are more reliable for narrowband components than broadband components, we can be confident of the accuracy of our results.

Phase disparity

The phase-disparity tuning of our components nonuniformly spans the range of possible angular values, suggesting that the full range of phase disparity could be used to detect disparities in the visual scene. However, phase disparities of $\pi/2$ are much less prevalent than disparities around 0 and π , implying that these disparities have less explanatory power.

The distribution of phase disparities was strongly bimodal (see Figure 6), with peaks at 0 and π radians. The peak at 0 radians indicates the detection of correlated signals in each view. As the phase disparity is partially independent of the position disparity, these correlated signals may be shifted in each view. The components around π radians are anticorrelated between the left and right eyes. Their presence is consistent with Li and Atick's (1994a) decorrelated-channels theory of binocular vision. The plus (correlated) and minus (anticorrelated) channels that decorrelate single-pixel sample inputs in their research are found in the interactions between multiple pixels in the ICA models as phase differences. As noted by Bell and Sejnowski (1997) and Ringach (2002), edge-like components produce sparse coding in the monocular case, locally decorrelating the images. The appearance of anticorrelated binocular sparse components is the logical extension of this to binocular image patches. The bias towards anticorrelated binocular components has been observed before in Fourier analysis by Li and Atick (1994a), and similar anticorrelated filters were also produced in Burge and Geisler's (2014) analysis of optimal filters for disparity estimation. Burge and Geisler noted that a particular anticorrelated component could signal the presence of a stimulus at a particular disparity by *not* responding. This is related to

the idea that such cells play an inhibitory role, vetoing possible disparities when they do respond strongly (Read & Cumming, 2007). Recently, an additional role for these anticorrelated cells in distinguishing object boundaries from texture edges has been suggested by Goutcher, Hunter, and Hibbard (2013).

Only half of this bimodal distribution has been found in physiological studies. Phase disparities in binocular cells of the macaque (Prince, Cumming, & Parker, 2002), cat (Anzai et al., 1999), and barn owl (Nieder & Wagner, 2000), as collated by Prince, Cumming, and Parker (2002), showed a clear bias towards phase disparities of 0 radians, but with few anticorrelated neurons. Although such "tuned inhibitory" neurons do exist (Poggio et al., 1985; Poggio & Fischer, 1977), they are not nearly as prevalent as would be predicted from the current analysis. We and previous authors have assumed that the visual cortex forms an efficient coding of the visual scene, but without any reference to the utility of the coding. In other words, neurons could code for stimuli that exist in the visual input but are not used in subsequent processing. This would be extremely energy inefficient. It is reasonable to assume that a pruning process could occur that selects for useful parts of the visual signal, although at present no biological process for such pruning is known. Analyses that are targeted at identifying the filters that are optimized for specific tasks, such as disparity estimation (Burge & Geisler, 2014) or scene parsing (Goutcher et al., 2013), can provide an additional level of understanding of the encoding of natural images.

Position disparity

Distributions of position-disparity tuning were highly peaked around 0. Components tuned to a disparity of less than half a wavelength dominate the distribution, with a clear majority tuned to a disparity of less than quarter of a wavelength. This result is qualitatively similar to neurophysiological measurements in V1 of macaques. Both Anzai et al. (1999) and Prince and colleagues (Prince, Cumming, & Parker, 2002; Prince, Pointon, et al., 2002) found that position disparities were mainly constrained to half the wavelength of the filter and clustered around 0. Finding this result in ICA components indicates that the relatively small position disparities found in animal studies form an efficient coding of binocular visual inputs, in line with geometrical considerations (Hibbard, 2007; Read & Cumming, 2004a). The distribution of tuning for vertical disparity was more strongly peaked at 0 than that for horizontal disparity, again in line with geometrical predictions (Hibbard, 2007; Read & Cumming, 2004b) and physiological findings (Cumming, 2002).

We do not have information about the range of disparities present in the images. It is, however, likely to be greater than the range of disparity tuning found in our components (between 2 [the Nyquist limit] and 8 arcmin; see Figure 15), since training patches were cut from both the verged and unverged regions of the image. We can conclude that although disparities greater than the wavelength of the filter are most likely present in the scenes, filters tuned to these disparities do not form an efficient coding. An explanation of this apparent discrepancy can be found in the fact that filters do not exclusively respond to object boundaries, but also encode object texture. Unlike object boundary edges, textures are frequently repetitive, and thus a disparity detector tuned to a particular frequency could make many good matches other than the correct disparity. As the ICA algorithm will find the most prevalent features regardless of actual disparity, the matches with the shortest distance between edges will dominate. While this results in an efficient encoding, this ambiguity needs to be resolved for the actual estimation of disparity. This highlights the important distinction between the initial encoding of binocular images in V1 (the stage that we seek to model here) and the subsequent estimation of disparity in higher cortical areas. It should also be noted that components tuned to larger disparities are present in ICA applied at coarser scales, consistent with the idea that larger disparities are detected by neurons with larger receptive fields (Allenmark & Read, 2011).

Orientation tuning and the direction of disparity

Cumming (2002) found no correlation between the orientation tuning of neurons and the direction of disparity to which they were most sensitive. The oval-shaped distribution of displacements shown in Figure 8A is similar to results found in monkeys (Cumming, 2002), where a similar bias towards detection of horizontal disparities was found. Like Cumming, we found no association between the direction of position disparity and the orientation of the components. It should be noted, however, that the strong effect of grid alignment found in the data might have masked any such association.

The relationship between phase- and position-disparity tuning

Physiological studies have found evidence of mixtures of phase- and position-disparity tuning. These tunings span a large proportion of the range of possible phase- and position-disparity combinations and were found to be uncorrelated. Similar to our results, neural tuning has been shown to cluster around 0 in both position and phase disparities (Anzai et al., 1999;

Prince, Cumming, & Parker, 2002; Prince, Pointon, et al., 2002).

We found a strong linear relationship between phase disparity and position disparity that implies joint use of phase- and position-disparity-tuned components in scene disparity calculations. This relationship can be explained by the similarities between Gabor functions shifted in phase and shifted in position (the basis of the Fourier shift theory). This result is intriguing. Rather than spanning the space of all possible phase and position disparities, the components are clustered at particular combinations that have particular combined disparity, specifically multiples of half the wavelength. This result has not been observed in image statistics by other authors (Burge & Geisler, 2014). Similarly, it has not been observed in physiological studies. Cumming and DeAngelis (2001) and Anzai et al. (1999) found a wide spread of phase and position disparities. Prince et al. did not convert their measurements into equivalent units and cannot be directly compared (Prince et al., 2002a). The phase and position distributions reported by these authors are marginal distributions combining results across a wide range of frequency tunings from broadband to narrowband. Our results are constrained in frequency tuning and are generally more narrowband tuned than physiological measurements. It is possible that the broader range of phase and position disparities measured in primates is a consequence of broad frequency-tuning functions, with narrowband-tuned cells exhibiting a similar distribution to one observed here.

Possible algorithms have been suggested to use these two measures of disparity. For example, Y. Chen and Qian (2004) used phase disparity to estimate local shifts and position disparity to confirm the results. In contrast, Read and Cumming (2007) used position disparity to calculate local shifts, and phase disparity to detect false positives. Read and Cumming claimed more accurate results for their method compared to Y. Chen and Qian. These algorithms assume that phase and position disparity are not correlated.

Scale

The range of disparities found across image scales (Figure 16) indicates a multiscale approach to the detection of disparity (Allenmark & Read, 2011). At each scale, the distribution of components spans a similar range of frequencies. A similar distribution was proposed mathematically by Li and Atick (1994b) to perform two functions on binocular images: noise reduction, especially at higher frequencies, and whitening of the input signals. The range of disparities detected by components at the different scales shares some features with Li and Atick's model. At each scale, the band-pass operation avoids signals close to the

Shannon–Nyquist limit, where high-frequency noise dominates the signal (Shannon, 1949). The range of frequencies detected also depends on the scale, with coarse scales detecting a wider range of frequencies and disparities than higher frequencies.

Discussion

We used ICA to produce a sparse linear coding of binocular image patches. This produced Gabor-like features which we analyzed in terms of phase and position disparity.

As have other authors, we found a range of phase- and position-disparity-coding components (Anzai et al., 1999; Okajima, 2004). Our analysis has produced many more, and more detailed, measurements than previous studies. As a result, we observed new relationships in the data. We found a linear relationship between phase and position disparity that produced components with highly clustered overall disparity profiles. This is different from the physiological measurements of Anzai et al. (1999) and Prince, Cumming, and Parker (2002), which show no correlation between phase- and position-disparity tunings. In terms of signal processing, our results show a clear link between narrowband phase and position disparities in each view.

Physiological measurements have found many fewer anticorrelated tuned neurons in V1 than predicted by our results (Prince, Cumming, & Parker, 2002). However, one important distinction is that such physiological measurements have been taken from cells with receptive fields in the center of the visual field, whereas the analysis presented here considers samples drawn from the whole image. While beyond the scope of the present article, it is possible that this discrepancy reflects the difference in spatial sampling.

Overall, there are a number of ways in which our ICA results produce components with properties that are similar to binocular cortical neurons. Our components are well fitted by Gabor functions with similar orientation and spatial-frequency tuning in each eye (Bridge & Cumming, 2001). These components showed position- and phase-disparity tuning, with most components having a combination of both (Prince, Cumming, & Parker, 2002). The distributions of horizontal and vertical position disparity were both strongly peaked around 0, with a greater spread for horizontal than for vertical disparity (Cumming, 2002; Hibbard, 2007; Read & Cumming, 2004b). There was also a local peak in the distribution of phase disparities around 0 (Prince, Cumming, & Parker, 2002).

There were however also a number of ways in which our results differed from physiological findings. Most

notably, the largest peak in the distribution of phase disparities was found at π . Also, when the preferred disparity of each component was calculated, by taking account of both its position and phase tuning, peaks in the distribution at half-wavelength intervals were evident. These unexpected results represent aspects of the components learned that do not directly reflect attributes of cortical neurons (Ringach, 2002).

The ICA algorithm detected features based on their prevalence in the supplied image set. Matches between these components and the images do not necessarily mean that the actual disparities of objects in the image match that of the component. It is likely that a proportion of these matches will be false—i.e., the matched disparities are not the same as the actual, physical disparities. The algorithm has a strong bias towards narrowband features with large receptive fields, while the visual cortices of cats and monkeys have a larger proportion of broadband features with relatively smaller receptive fields (Ringach, 2002). In our analysis the components had a median frequency bandwidth of ~ 0.5 octaves; this differs from the median of 1.4 octaves reported by DeValois et al. (1982). Thus we have been comparing narrowband-tuned ICA components to the marginal statistics of features measured from V1 simple cells of a wide range of narrow- to broadband tunings. The similarities we found have not been restricted to narrowband features in V1, suggesting that these features are not dependent on the bandwidth of the Gabor function. However, the differences that we have observed may be due in part to the size of the receptive fields and only hold for narrowband signals.

Taken on their own, the components calculated via ICA cannot calculate disparity. ICA is simply an efficient coding method, and simple correlations between the scene and components will produce many false matches. Algorithms based on the standard energy model combine the outputs of two or more components, with a nonlinear term, as the initial stage of disparity detection. The original model of Fleet et al. (1996) combined pairs of components with 0 position and $\pi/2$ phase shift while also pooling information across orientation, scale, and spatial position. Numerous possible combinations of components have been suggested, including multiscale phase-based models (Y. Chen & Qian, 2004), a gated model where phase maxima close to 0 are combined with position extrema (Read & Cumming, 2007), combining positive- and negative-energy model units (Haefner & Cumming, 2005), and filters based on learning the appropriate combinations from natural-image data (Burge & Geisler, 2014). Whatever combination of binocularly encoded information is required for the estimation of disparity, this is likely to occur in visual areas beyond V1.

Our results, in line with previous studies, reveal some clear similarities between the components learned and the receptive fields of cortical neurons, but also a number of differences. This highlights the limitations of trying to explain these receptive-field properties as the result of the encoding principles employed. One important limitation is that the result might reflect properties of the learning methods employed, such as image sampling and preprocessing, that do not reflect the relevant encoding principles, such as independence (Bell & Sejnowski, 1997; Ringach, 2002; van Hateren & van der Schaaf, 1998). Another important consideration is that the properties of cortical neurons are likely to be determined not by considerations of how to encode information so as to generate a full representation of the image (Ringach, 2002) but by how this information will subsequently be used, for example in the estimation of disparity (Burge & Geisler, 2014).

Another important limitation of our approach, in line with many other approaches to understanding efficient coding, is that it does not explicitly consider noise in either the input signal or neural responses (Simoncelli & Olshausen, 2001). The levels of both forms of noise are important factors in determining an efficient encoding (for a detailed discussion, see Zhaoping, 2014). Consideration of noise has contributed to our understanding of the efficient coding of information in the retina (Atick & Redlich, 1990, 1992) and in binocular vision (Li & Atick, 1994a), for example. The approach to learning independent components does, however, have some advantages from a consideration of the signal-to-noise ratio. Firstly, as discussed in the methods section, the PCA whitening stage—in which later, higher frequency components are truncated—bears some similarity to the explanation of retinal encoding proposed by Atick and Redlich (1992), in which noise is shown to dominate the signal at high frequencies (due to the $1/f^2$ power spectrum typical of natural images) and truncation of the signal to lower frequencies increases the signal-to-noise ratio. Secondly, Field (1987, 1994) has argued that in the context of uncorrelated signal noise, sparse coding may increase the signal-to-noise ratio, as neurons will respond selectively to a subset of the signal space while uniform white noise is distributed across the entire space of possible signals. However, as Hyvärinen et al. (1999) have pointed out, an ICA model trained on noisy input data will produce components tuned selectively to respond to a single (or nearly single) sample. In our work we have used bootstrapping in an attempt to assess the impact such outliers have on the distributions of components learned from ICA.

A final consideration is that, while the methods we used to calculate components have the aim of producing a sparse encoding, alternative metrics exist.

Einhäuser, Kayser, König, and Körding (2002) used a method that attempted to maximize temporal stability, arguing that this was necessary for learning the features of complex cells but not for learning simple-cell responses. It should be noted that although not explicitly referred to by Einhäuser et al., this learning method was sparse in that only a subset of inputs was used for learning in any given iteration. The idea of temporal stability was also explored by Hurri and Hyvärinen (2003) using a different method that was nonsparse. Other statistical models exist that have demonstrable efficacy in describing natural images, in many cases outperforming ICA in terms of image data explained (log likelihood; Zoran & Weiss, 2012). The class of models known as mixture models has received a significant amount of attention; variations on these models have been shown to outperform ICA. Both Gaussian scale models (Lyu & Simoncelli, 2007) and Gaussian mixture models (Xu & Jordan, 1996) have been found to be better descriptors of natural-image patches in terms of their likelihood. Mixtures of elliptically contoured distributions have been shown psychophysically to produce more natural-looking image patches (Gerhard, Wichmann, & Bethge, 2013). However, unlike factor models such as ICA, mixture models do not produce sets of individual components with which to compare to physiology; instead, they produce linearly additive mixtures of distributions with no direct physiological analogue.

Keywords: binocular vision, binocular disparity, natural-image statistics, independent-component analysis

Acknowledgments

This work was supported by the Engineering and Physical Sciences Research Council Strategic Partnership Funds 2012–13 with the University of St Andrews, UK; and the Biotechnology and Biological Sciences Research Council (grant number BB/K018973/1).

Commercial relationships: none.

Corresponding author: David W. Hunter.

Email: dwh5@st-andrews.ac.uk.

Address: School of Psychology and Neuroscience, St Andrews, Fife, UK.

Footnote

¹ Binocular photographic image data and (MATLAB) source code associated with this publication are available at <https://github.com/DavidWilliamHunter/Bivis>.

References

- Allenmark, F., & Read, J.C.A. (2011). Spatial stereo-resolution for depth corrugations may be set in primary visual cortex. *PLoS Computational Biology*, 7(8), e1002142, doi:10.1371/journal.pcbi.1002142.
- Anzai, A., Ohzawa, I., & Freeman, R. D. (1999). Neural mechanisms for encoding binocular disparity: Receptive field position versus phase. *Journal of Neurophysiology*, 82, 874–890.
- Atick, J. J., & Redlich, A. N. (1990). Towards a theory of early visual processing. *Neural Computation*, 2(3), 308–320.
- Atick, J. J., & Redlich, A. N. (1992). What does the retina know about natural scenes? *Neural Computation*, 4(2), 196–210.
- Barlow, H. B. (1961). Possible principles underlying the transformation of sensory messages. *Sensory Communication*, 217–234.
- Bell, A. J., & Sejnowski, T. J. (1997). The “independent components” of natural scenes are edge filters. *Vision Research*, 37(23), 3327–3338.
- Berens, P. (2009). CircStat: A MATLAB toolbox for circular statistics. *Journal of Statistical Software*, 31(10), 1–21.
- Blakemore, C., Fiorentini, A., & Maffei, L. (1972). A second neural mechanism of binocular depth discrimination. *The Journal of Physiology*, 226(3), 725–749.
- Bridge, H., & Cumming, B. G. (2001). Responses of macaque V1 neurons to binocular orientation differences. *The Journal of Neuroscience*, 21(18), 7293–7302.
- Bridge, H., Cumming, B. G., & Parker, A. (2001). Psychophysical evidence against the use of orientation disparity in the perception of slant. *Journal of Vision*, 1(3): 172, doi:10.1167/1.3.172. [Abstract].
- Burge, J., & Geisler, W., S., (2014). Optimal disparity estimation in natural stereo-images. *Journal of Vision*, 14(2):1, 1–18, doi:10.1167/14.2.1. [PubMed] [Article].
- Chen, D., & Li, Z. (1998). A psychophysical experiment to test the efficient stereo coding theory. Paper presented at *Theoretical aspects of neural computation: a multidisciplinary perspective: International Workshop, TANC '97*, Hong Kong, 26–28 May 1997 (pp. 225–235). Berlin: Springer-Verlag.
- Chen, Y., & Qian, N. (2004). A coarse-to-fine disparity energy model with both phase-shift and position-shift receptive field mechanisms. *Neural Computation*, 16, 1545–1577, doi:10.1162/089976604774201596.
- Clarke, P., Donaldson, I., & Whitteridge, D. (1976). Binocular visual mechanisms in cortical areas I and II of the sheep. *The Journal of Physiology*, 256(3), 509–526.
- Croner, L. J., & Kaplan, E. (1995). Receptive fields of P and M ganglion cells across the primate retina. *Vision Research*, 35(1), 7–24.
- Cumming, B. G. (2002). An unexpected specialization for horizontal disparity in primate primary visual cortex. *Nature*, 418(6898), 633–636.
- Cumming, B. G., & DeAngelis, G. C. (2001). The physiology of stereopsis. *Annual Review of Neuroscience*, 24, 203–238.
- DeAngelis, G. C., Ohzawa, I., & Freeman, R. D. (1991). Depth is encoded in the visual cortex by a specialized receptive field structure. *Nature*, 352(6331), 156–159.
- DeAngelis, G. C., Ohzawa, I., & Freeman, R. D. (1995). Neuronal mechanisms underlying stereopsis: How do simple cells in the visual cortex encode binocular disparity? *Perception*, 24(1), 3–31.
- DeAngelis, G. C., & Uka, T. (2003). Coding of horizontal disparity and velocity by MT neurons in the alert macaque. *Journal of Neurophysiology*, 89(2), 1094–1111.
- DeValois, R. L., Albrecht, D. G., & Thorell, L. G. (1982). Spatial frequency selectivity of cells in macaque visual cortex. *Vision Research*, 22, 545–559, doi:10.1016/0042-6989(82)90113-4.
- Ding, J., & Sperling, G. (2006). A gain-control theory of binocular combination. *Proceedings of the National Academy of Sciences, USA*, 103(4), 1141–1146.
- Durand, J.-B., Zhu, S., Celebrini, S., & Trotter, Y. (2002). Neurons in parafoveal areas V1 and V2 encode vertical and horizontal disparities. *Journal of Neurophysiology*, 88(5), 2874–2879.
- Einhäuser, W., Kayser, C., König, P., & Körding, K. P. (2002). Learning the invariance properties of complex cells from their responses to natural stimuli. *European Journal of Neuroscience*, 15(3), 475–486.
- Faria, F. da C. e C., Batista, J., & Araújo, H. (2013). Stereoscopic depth perception using a model based on the primary visual cortex. *PLoS ONE*, 8(12), e80745, doi:10.1371/journal.pone.0080745.
- Field, D. J. (1994). What is the goal of sensory coding? *Neural Computation*, 6(4), 559–601.
- Field, D. J. (1987). Relations between the statistics of natural images and the response properties of

- cortical cells. *Journal of the Optical Society of America A*, 4(12), 2379–2394.
- Field, D. J., & Chandler, D. M. (2012). Method for estimating the relative contribution of phase and power spectra to the total information in natural-scene patches. *Journal of the Optical Society of America A*, 29(1), 55–67.
- Fischer, S., Sroubek, F., Perrinet, L., Redondo, R., & Cristóbal, G. (2007). Self invertible log-Gabor wavelets. *International Journal of Computer Vision*, 75, 231–246.
- Fleet, D. J., Wagner, H., & Heeger, D. J. (1996). Neural encoding of binocular disparity: Energy models, position shifts and phase shifts. *Vision Research*, 36(12), 1839–1857.
- Freeman, R. D., & Ohzawa, I. (1990). On the neurophysiological organisation of binocular vision. *Vision Research*, 30, 1661–1676.
- Geisler, W. S., Najemnik, J., & Ing, A.D. (2009). Optimal stimulus encoders for natural tasks. *Journal of Vision*, 9(13):17, 1–16, doi:10.1167/9.13.17. [PubMed] [Article].
- Gerhard, H. E., Wichmann, F. A., & Bethge, M. (2013). How sensitive is the human visual system to the local statistics of natural images? *PLoS Computational Biology*, 9(1), e1002873.
- Gonzalez, F., Justo, M. S., Bermudez, M. A., & Perez, R. (2003). Sensitivity to horizontal and vertical disparity and orientation preference in areas V1 and V2 of the monkey. *NeuroReport*, 14(6), 829–832.
- Goutcher, R., Hunter, D. W., & Hibbard, P. B. (2013). Tuned inhibitory responses in binocular natural images. *i-Perception*, 4(7), 484–484.
- Graham, D. J., Chandler, D. M., & Field, D. J. (2006). Can the theory of “whitening” explain the center-surround properties of retinal ganglion cell receptive fields? *Vision Research*, 46(18), 2901–2913.
- Greenwald, H. S., & Knill, D. C. (2009). Orientation disparity: A cue for 3D orientation? *Neural Computation*, 21(9), 2581–2604.
- Haefner, R., & Cumming, B. G. (2005). Spatial nonlinearities in V1 disparity-selective neurons. *Society for Neuroscience Abstracts*, 583.9.
- Hampton, D. R., & Kertesz, A. E. (1983). The extent of Panum’s area and the human cortical magnification factor. *Perception*, 12(2), 161–165.
- Hansen, B. C., & Essock, E. A. (2004). A horizontal bias in human visual processing of orientation and its correspondence to the structural components of natural scenes. *Journal of Vision*, 4(12):5, 1044–1060, doi:10.1167/4.12.5. [PubMed] [Article].
- Hawken, M. J., & Parker, A. J. (1987). Spatial properties of neurons in the monkey striate cortex. *Proceedings of the Royal Society of London B: Biological Sciences*, 231(1263), 251–288.
- Heydt, R., Adorjani, C., Hányi, P., & Baumgartner, G. (1978). Disparity sensitivity and receptive field incongruity of units in the cat striate cortex. *Experimental Brain Research*, 31(4), 523–545.
- Hibbard, P. B. (2007). A statistical model of binocular disparity. *Visual Cognition*, 15(2), 149–165.
- Hibbard, P. B. (2008). Binocular energy responses to natural images. *Vision Research*, 48(12), 1427–1439.
- Himberg, J., Hyvärinen, A., & Esposito, F. (2004). Validating the independent components of neuro-imaging time series via clustering and visualization. *NeuroImage*, 22(3), 1214–1222.
- Hong, G., Luo, M. R., & Rhodes, P. A. (2001). A study of digital camera colorimetric characterization based on polynomial modeling. *Color Research & Application*, 26(1), 76–84.
- Howard, I. P. (2002). *Seeing in depth, Vol. 1: Basic mechanisms*. Toronto, Canada: University of Toronto Press.
- Howard, I. P., & Rogers, B. J. (2002). *Seeing in depth, Vol. 2: Depth perception*. Toronto, Canada: University of Toronto Press.
- Hoyer, P. O., & Hyvärinen, A. (2000). Independent component analysis applied to feature extraction from colour and stereo images. *Network: Computation in Neural Systems*, 11(3), 191–210.
- Hubel, D. H., & Wiesel, T. N. (1962). Receptive fields, binocular interaction and functional architecture in the cat’s visual cortex. *The Journal of Physiology*, 160, 106–154.
- Hurri, J., & Hyvärinen, A. (2003). Simple-cell-like receptive fields maximize temporal coherence in natural video. *Neural Computation*, 15(3), 663–691.
- Hyvärinen, A. (1999). Fast and robust fixed-point algorithms for independent component analysis. *IEEE Transactions on Neural Networks*, 10(3), 626–634.
- Hyvärinen, A. (2013). Independent component analysis: recent advances. *Philosophical Transactions of the Royal Society of London A: Mathematical, Physical and Engineering Sciences*, 371(1984), 1–19.
- Hyvärinen, A., Hurri, J., & Hoyer, P. O. (2009). *Natural image statistics: A probabilistic approach to early computational vision* (Vol. 39). New York: Springer-Verlag.
- Hyvärinen, A., Särelä, J., & Vigário, R. (1999). Spikes and bumps: Artefacts generated by independent component analysis with insufficient sample size.

- Proceedings of the International Workshop on Independent Component Analysis and Signal Separation (ICA'99)* (pp. 425–429). Aussois, France.
- Jammalamadaka, S., & Sengupta, A. (2001). *Topics in circular statistics*. River Edge, N.J.: World Scientific.
- Laughlin, S. (1981). A simple coding procedure enhances a neuron's information capacity. *Zeitschrift für Naturforschung*, *36*, 910–912.
- LeVay, S., & Voigt, T. (1988). Ocular dominance and disparity coding in cat visual cortex. *Visual Neuroscience*, *1*(4), 395–414.
- Li, Z., & Atick, J. J. (1994a). Efficient stereo coding in the multiscale representation. *Network: Computation in Neural Systems*, *5*(2), 157–174.
- Li, Z., & Atick, J. J. (1994b). Toward a theory of the striate cortex. *Neural Computation*, *6*(1), 127–146.
- Liu, Y., Bovik, A. C., & Cormack, L. K. (2008). Disparity statistics in natural scenes. *Journal of Vision*, *8*(11):19, 1–14, doi:10.1167/8.11.19. [PubMed] [Article].
- Lyu, S., & Simoncelli, E. P. (2006). Statistical modeling of images with fields of Gaussian scale mixtures. *Advances in Neural Information Processing Systems*, *19*, 945–952.
- May, K. A., Zhaoping, L., & Hibbard, P. B. (2012). Perceived direction of motion determined by adaptation to static binocular images. *Current Biology*, *22*, 28–32.
- Nelder, J. A., & Mead, R. (1965). A simplex method for function minimization. *The Computer Journal*, *7*(4), 308–313.
- Nelson, J., Kato, H., & Bishop, P. (1977). Discrimination of orientation and position disparities by binocularly activated neurons in cat striate cortex. *Journal of Neurophysiology*, *40*(2), 260–283.
- Neri, P. (2005). A stereoscopic look at visual cortex. *Journal of Neurophysiology*, *93*(4), 1823–1826.
- Nieder, A., & Wagner, H. (2000). Horizontal-disparity tuning of neurons in the visual forebrain of the behaving barn owl. *Journal of Neurophysiology*, *83*(5), 2967–2979.
- Nikara, T., Bishop, P., & Pettigrew, J. (1968). Analysis of retinal correspondence by studying receptive fields of binocular single units in cat striate cortex. *Experimental Brain Research*, *6*(4), 353–372.
- Ninio, J. (1985). Orientational versus horizontal disparity in the stereoscopic appreciation of slant. *Perception*, *14*(3), 305–314.
- Ohzawa, I., DeAngelis, G. C., & Freeman, R. D. (1990, August). Stereoscopic depth discrimination in the visual cortex: Neurons ideally suited as disparity detectors. *Science*, *249*(4972), 1037–1041.
- Ohzawa, I., DeAngelis, G. C., & Freeman, R. D. (1996). Reply. *Trends in Neurosciences*, *19*(9), 386.
- Ohzawa, I., DeAngelis, G. C., & Freeman, R. D. (1997). Encoding of binocular disparity by complex cells in the cat's visual cortex. *Journal of Neurophysiology*, *77*(6), 2879–2909.
- Okajima, K. (2004). Binocular disparity encoding cells generated through an infomax based learning algorithm. *Neural Networks*, *17*(7), 953–962, doi:10.1016/j.neunet.2004.02.004.
- Olshausen, B. (2002). Sparse codes and spikes. In R. P. N. Rao, B. A. Olshausen, & M. S. Lewicki (Eds.), *Probabilistic models of the brain: Perception and neural function* (pp. 257–272). Cambridge, MA: MIT Press.
- Olshausen, B. A., & Field, D. J. (1996). Natural image statistics and efficient coding. *Network: Computation in Neural Systems*, *7*(2), 333–339.
- Parker, A. J. (2007). Binocular depth perception and the cerebral cortex. *Nature Reviews Neuroscience*, *8*(5), 379–391.
- Pettigrew, J. D. (1972). The neurophysiology of binocular vision. *Scientific American*, *227*(2), 84–95.
- Pettigrew, J. D., & Konishi, M. (1976). Neurons selective for orientation and binocular disparity in the visual wulst of the barn owl (*Tyto alba*). *Science*, *193*(4254), 675–678.
- Poggio, G. (1991). Physiological basis of stereoscopic vision. In *Vision and visual dysfunction: binocular vision and psychophysics* (Vol. 9, pp. 227–238). London: Macmillan Press.
- Poggio, G. F., & Fischer, B. (1977). Binocular interaction and depth sensitivity in striate and prestriate cortex of behaving rhesus monkey. *Journal of Neurophysiology*, *40*(6), 1392–1405.
- Poggio, G. F., Gonzalez, F., & Krause, F. (1988). Stereoscopic mechanisms in monkey visual cortex: Binocular correlation and disparity selectivity. *The Journal of Neuroscience*, *8*(12), 4531–4550.
- Poggio, G. F., Motter, B. C., Squatrito, S., & Trotter, Y. (1985). Responses of neurons in visual cortex (V1 and V2) of the alert macaque to dynamic random-dot stereograms. *Vision Research*, *25*(3), 397–406.
- Poggio, G. F., & Talbot, W. H. (1981). Mechanisms of static and dynamic stereopsis in foveal cortex of the rhesus monkey. *The Journal of Physiology*, *315*(1), 469–492.
- Porrill, J., Ivins, J. P., & Frisby, J. P. (1999). The

- variation of torsion with vergence and elevation. *Vision Research*, 39(23), 3934–3950.
- Prince, S. J. P., Cumming, B. G., & Parker, A. J. (2002). Range and mechanism of encoding of horizontal disparity in macaque V1. *Journal of Neurophysiology*, 87(1), 209–221.
- Prince, S. J. P., Pointon, A., Cumming, B. G., & Parker, A. J. (2002). Quantitative analysis of the responses of V1 neurons to horizontal disparity in dynamic random-dot stereograms. *Journal of Neurophysiology*, 87(1), 191–208.
- Qin, D., Takamatsu, M., & Nakashima, Y. (2006). Changing binocular fusional area with retinal shift in binocular vision. *Journal of Light & Visual Environment*, 30(1), 29–33.
- Read, J. C. A., & Cumming, B. G. (2003). Testing quantitative models of binocular disparity selectivity in primary visual cortex. *Journal of Neurophysiology*, 90, 2795–2817.
- Read, J. C. A., & Cumming, B. G. (2004a). Ocular dominance predicts neither strength nor class of disparity selectivity with random-dot stimuli in primate V1. *Journal of Neurophysiology*, 91, 1271–1281.
- Read, J. C. A., & Cumming, B. G. (2004b). Understanding the cortical specialization for horizontal disparity. *Neural Computation*, 16(10), 1983–2020.
- Read, J. C. A., & Cumming, B. G. (2007). Sensors for impossible stimuli may solve the stereo correspondence problem. *Nature Neuroscience*, 10(10), 1322–1328.
- Ringach, D. L. (2002). Spatial structure and symmetry of simple-cell receptive fields in macaque primary visual cortex. *Journal of Neurophysiology*, 88, 455–463.
- Ringach, D. L., Sapiro, G., & Shapley, R. (1997). A subspace reverse-correlation technique for the study of visual neurons. *Vision Research*, 37(17), 2455–2464.
- Roe, A. W., Parker, A. J., Born, R. T., & DeAngelis, G. C. (2007). Disparity channels in early vision. *The Journal of Neuroscience*, 27(44), 11820–11831.
- Shannon, C. E. (1949). Communication in the presence of noise. *Proceedings of the IRE*, 37(1), 10–21.
- Simoncelli, E. P., & Olshausen, B. A. (2001). Natural image statistics and neural representation. *Annual Review of Neuroscience*, 24, 1193–1216, doi:10.1146/ANNUREV.NEURO.24.1.1193.
- Srinivasan, M., Laughlin, S., & Dubs, A. (1982). Predictive coding: A fresh view of inhibition in the retina. *Proceedings of the Royal Society of London B: Biological Sciences*, 216(1205), 427–459.
- Tong, L., Guido, W., Tumosa, N., Spear, P. D., & Heidenreich, S. (1992). Binocular interactions in the cat's dorsal lateral geniculate nucleus: II. Effects on dominant-eye spatial-frequency and contrast processing. *Visual Neuroscience*, 8(6), 557–566.
- Tsao, D. Y., Conway, B. R., & Livingstone, M. S. (2003). Receptive fields of disparity-tuned simple cells in macaque V1. *Neuron*, 38(1), 103–114. doi:10.1016/S0896-6273(03)00150-8.
- Tyler, C. W., & Sutter, E. E. (1979). Depth from spatial frequency difference: An old kind of stereopsis? *Vision Research*, 19(8), 859–865.
- van der Schaaf, A., & van Hateren, J. H. (1996). Modelling the power spectra of natural images: Statistics and information. *Vision Research*, 36(17), 2759–2770.
- van Hateren, J. H., & van der Schaaf, A. (1998). Independent component filters of natural images compared with simple cells in primary visual cortex. *Proceedings of the Royal Society of London B: Biological Sciences*, 265(1394), 359–366.
- Wieniawa-Narkiewicz, E., Wimborne, B., Michalski, A., & Henry, G. (1992). Area 21a in the cat and the detection of binocular orientation disparity. *Ophthalmic and Physiological Optics*, 12(2), 269–272.
- Xu, L., & Jordan, M. I. (1996). On convergence properties of the EM algorithm for Gaussian mixtures. *Neural Computation*, 8(1), 129–151.
- Zhaoping, L. (2014). *Understanding vision: Theory, models, and data*. Oxford, UK: Oxford University Press.
- Zoran, D., & Weiss, Y. (2012). Natural images, Gaussian mixtures and dead leaves. In *Advances in Neural Information Processing Systems* (pp. 1736–1744).